| | |
|---|---|
| Title | Control of Spin-Dependent Quantum Interference in Magnetic Tunnel Junctions with Fe Ultrathin Layer |
| Author(s) | Sheng, Peng |
| Citation | 大阪大学, 2013, 博士論文 |
| Version Type | VoR |
| URL | https://hdl.handle.net/11094/27499 |
| rights | |
| Note | |

# Control of Spin-Dependent Quantum Interference in Magnetic Tunnel Junctions with Fe Ultrathin Layer

SHENG PENG

MARCH 2013

# Control of Spin-Dependent Quantum Interference in Magnetic Tunnel Junctions with Fe Ultrathin Layer

A dissertation submitted to

THE GRADUATE SCHOOL OF ENGINEERING SCIENCE

OSAKA UNIVERSITY

in partial fulfillment of the requirements for the degree of

DOCTOR OF PHILOSOPHY IN ENGINEERING

BY

SHENG PENG

MARCH 2013

# ABSTRACT

Electron confinement in quantum wells (QWs) has been extensively studied in semiconductor and metallic heterostructures. It has proven to be a powerful approach to tuning the electronic structure and to tailoring new functionalities in devices such as interlayer exchange coupling between ferromagnets. Quantum confinement of spin polarized electrons is therefore of great interest for both fundamental and applied spintronics. The work presented in this thesis focuses on spin- dependent quantum interference in Cr/ultrathin Fe/MgO/Fe MTJs. The goal of the research work in this thesis is to understand and control this phenomenon.

To give basic background knowledge of the main work in this thesis, brief introduction about the related research progress so far is presented in Chapter 1.

In Chapter 2, I describe the experimental method and equipment in detail.

The main work is presented in Chapter 3.

In Chapter 3.1, I present my experiment results about quantum well resonant peak positions versus the continuous Fe thickness, indicating a clear signature of quantum well states in the ultrathin Fe (001) electrode, confirmed the discrepancy in experiment and first-principle theoretical calculation. The correlation of the majority $\Delta_1$ band in the $\Gamma$ –H dispersion of bcc Fe and periodicity of resonant peak was also studied in details.

To investigate the origin of the discrepancy discussed in Chapter 3.1, in Chapter 3.2 I describe experimental results on Fe/MgO and Cr/Fe interface, and illustrate the influence of interface on quantum well resonant peak positions.

In Chapter 3.3 I report the influence of quantum interference on modulation TMR ratio in MTJs with the change of voltage and ultrathin Fe electrode thickness. In addition, the role of growth conditions and interface flatness in quantum well effect was also been investigated and discussed.

Conclusions are discussed in Chapter 4. We convince that control of spin dependent quantum well effect in MTJs with ultrathin Fe can be realized by precisely modifying the interface status, choosing the appropriate Fe thickness or voltage applied. This study paves the way for developing new functionalities in spintronics industry applications.

## *CONTENTS*

# CHAPTER 1 INTRODUCTION

## 1.1 Magnetic Tunnel Junctions (MTJs) with MgO Barrier

Magnetic Tunneling Junction (MTJ) is composed of two parallel conducting ferromagnetic layers separated by an insulating layer (a tunnel barrier). The resistance between the upper and the lower contact depends on the relative magnetization of the two ferromagnetic layers. The observed MR ratios were very small at first. The TMR effect was first observed by Julliere in 1975. He found that that Fe/Ge–O/Co MTJ exhibited a MR ratio of 14% at 4.2 K [1]. Until 1995, Miyazaki et al. [2] and Moodera et al. [3] observed a large TMR ratio (~18%) at room temperature (RT) in Fe/Al–O/Fe structure, and then it has attracted great and sustained attention because of its wide potential application in industry such as sensors and memory storage devices in the near future. Although RT MR ratios have been increased to about 81% by optimizing the ferromagnetic electrode materials and the conditions for fabricating the Al–O barrier [4], they are still not high enough for many applications of spintronic devices. High density magnetoresistive random access memory (MRAM) cells, for example, will need to have MR ratios that are higher than 150% at RT, and the read head in the next generation ultrahigh-density HDD will need to have both a high MR ratio and an ultralow tunneling resistance. The MR ratios of the conventional Al–O-based MTJs are simply not high enough for next-generation device applications. In 2001, first-principle calculations predicted that epitaxial MTJs with a crystalline magnesium oxide (MgO) tunnel barrier would have MR ratios over 1000% [5,6]. Following predictions by first-principles theory of a giant TMR effect in single-crystal Fe/MgO/Fe MTJs in 2001, MgO-based MTJs with a TMR ratio of about 200% at RT were reported by twp groups in 2004: CoFe/MgO/CoFe MTJs deposited by magnetron sputtering [7] and Fe/MgO/Fe MTJs epitaxially grown by molecular beam epitaxy (MBE) [8], respectively (see Fig. 1.1). From then, this subject has been boosted and drew the worldwide attention of researchers in MgO-based MTJs and MgO-based spin transfer torque devices. The MgO barrier has a single-crystal structure, instead of the amorphous structure of Al–O barrier. These large TMR ratios are determined by the different tunneling mechanisms and symmetry-related decay rates of the Bloch waves for the majority and the minority spin channels. The single-crystal MgO barrier exhibits a spin filtering effect due to the conservation of wave-function symmetry. The conductance in the P configuration, dominated by the majority $\Delta_1$ states, is high because $\Delta_1$ states decay relatively slowly through the barrier and can transfer into similar symmetry states in the second FM electrode. By contrast, the AP conductance is low due to the absence of receptor states in the second electrode (symmetry blocking), leading to giant MR ratio in MgO-based MTJs. The huge TMR effect in MgO based MTJs is now called the giant TMR effect and is of great importance not only for device applications but also for clarifying the physics of spin-dependent tunneling.

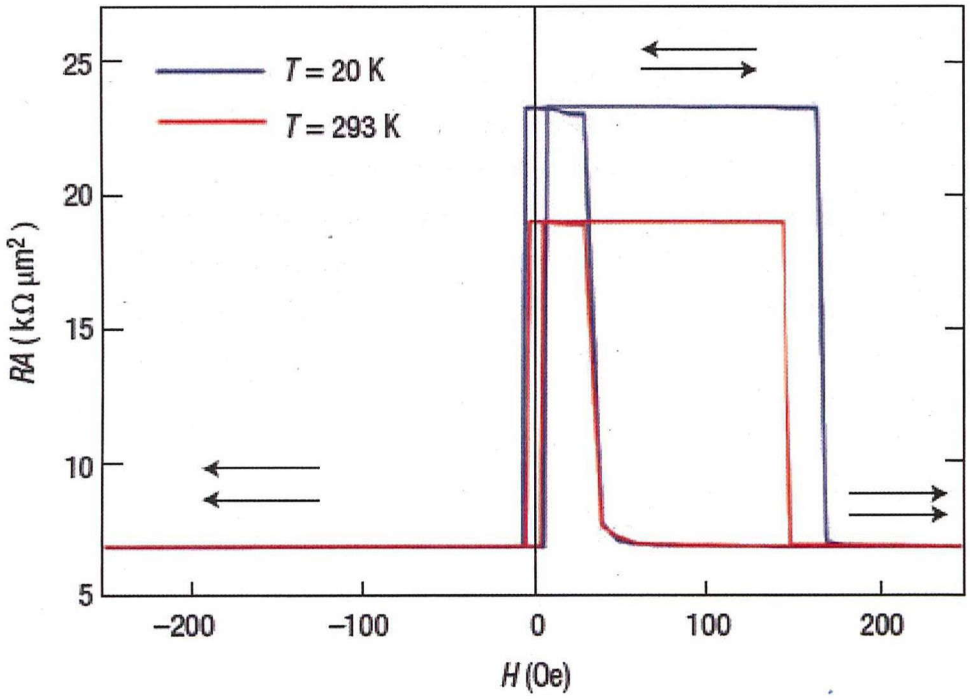

**Fig. 1.1**

Tunnel magnetoresistance of Fe(001)/MgO(001)/Fe(001) junctions. The Magnetoresistance curves measured at a bias voltage of 10 mV at T = 293 K and 20 K (MgO thickness is 2.3 nm). The resistance–area product RA plotted here is the tunnel resistance for a 1 × 1 μm area. Arrows indicate magnetization configurations of the top and bottom Fe electrodes. The MR ratio is 180% at 293 K and 247% at 20 K.

## 1.2 Coherent Tunneling in Single-Crystal Fe/MgO/Fe MTJs

The details of coherent tunneling through a crystalline MgO(001) barrier will be explained based on Fe/MgO/Fe MTJs in this chapter, since the author's research based on the Fe/MgO/Fe MTJs. In addition, the fully epitaxial Fe/MgO/Fe MTJs is also a good model for investigating the mechanism of spin-dependent tunneling transport due to the well defined crystal structure and magnetic properties.

First of all, we explain an incoherent tunneling process through the amorphous Al–O tunnel barrier. Tunneling in a MTJ with an amorphous Al–O barrier is illustrated schematically in Fig. 1.2 (a), where the top electrode layer is Fe(001) as an example of a 3d ferromagnet. Various Bloch states with different orbital symmetries exist in the electrodes. Because the Al–O tunnel barrier is amorphous, there is no crystallographic symmetry in the tunnel barrier and at the barrier/electrode interfaces. Because of this nonsymmetrical structure, Bloch states with various symmetries can couple with evanescent states (decaying tunneling states) in Al–O and therefore have finite tunneling probabilities. This tunneling process can be regarded as an incoherent tunneling.

For the Fe/MgO/Fe MTJs case, crystalline MgO(001) barrier layer can be epitaxially grown on a bcc Fe(001) layer with a rotation by 45° of the MgO lattice with respect to the Fe one, provides the symmetry conservation across the junction stack. Small lattice mismatch (3%) which can be absorbed by lattice distortions in the Fe and MgO layers and by the dislocations at their interface. Coherent tunneling transport in epitaxial Fe(001)/ MgO(001)/Fe(001) MTJ is illustrated schematically in Fig. 1.2 (b). In the case of ideal coherent tunneling, Fe $\Delta_1$ states are theoretically expected to dominantly tunnel through the MgO(001) barrier. The real space and reciprocal space representation of the bcc Fe lattice can be seen in Fig 1.3 (a) and Fig 1.3 (b) [9]. It can be easily illustrated by the following mechanism. There are three kinds of evanescent states (tunneling states) in the band gap of MgO(001): $\Delta_1$, $\Delta_5$, and $\Delta_{2'}$. Tunneling states actually have specific orbital symmetries and band dispersions. When the symmetries of tunneling wave functions are conserved, Fe $\Delta_1$ Bloch states couple with MgO $\Delta_1$ evanescent states. Fig 1.4 shows the partial DOS (obtained from first-principle calculations) for the decaying evanescent states in a MgO barrier layer at parallel magnetic configuration. Among these states, the $\Delta_1$ evanescent states have the slowest decay. The dominant tunneling channel for parallel magnetic state is therefore Fe $\Delta_1 \leftrightarrow$ MgO $\Delta_1 \leftrightarrow$ Fe $\Delta_1$. Band dispersion of bcc Fe for the (001) ($k_\parallel = 0$) direction is shown in Fig. 1.5. The *net* spin polarization of Fe is small because both majority- and minority-spin bands have many states at $E_F$, but the Fe $\Delta_1$ band is fully spin-polarized at $E_F$ ($P = 1$). A very large TMR effect in the epitaxial Fe(001)/MgO(001)/Fe(001) MTJ is therefore expected when $\Delta_1$ electrons dominantly tunnel. What should be noted that a finite tunneling current still flows though for antiparallel magnetic states [10].

Tunneling probability as a function of $k_\parallel$ wave vectors ($k_x$ and $k_y$) is shown in Fig. 1. 6. For the majority-spin conductance channel in the parallel magnetic state (P state) [Fig. 1.5(a)], tunneling takes place dominantly at $k_\parallel = 0$ because of the coherent tunneling of majority-spin $\Delta_1$ states. For the minority-spin conductance channel in the P state [Fig. 1.5(b)] and the conductance channel in antiparallel magnetic state (AP state) [Fig. 1.5(c)], spikes of tunneling probability appear at finite $k_\parallel$ points called *hot spots*. This *hot-spot tunneling* is resonant tunneling between interface resonant states [5,6]. Although a finite tunneling current flows through the hot spots in the AP state, the majority-spin conductance in the P state is much larger than that in the AP state, making the MR ratio very high [10].

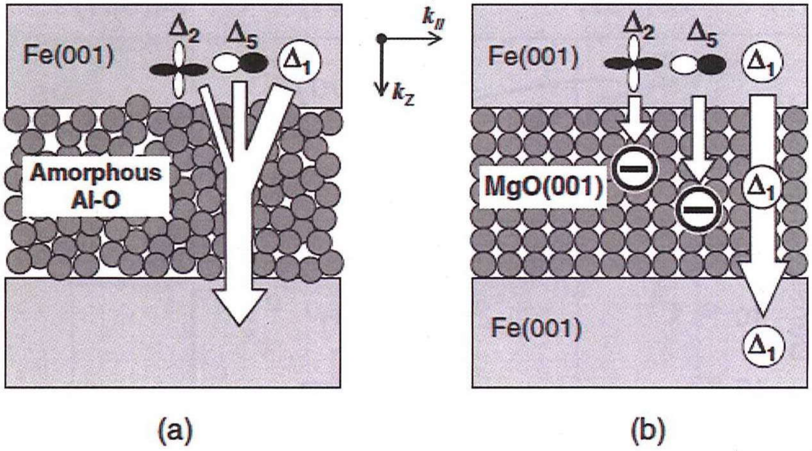

**Fig. 1.2**

Schematic illustrations of electron tunneling through (a) an amorphous Al–O barrier and(b) a crystalline MgO(001) barrier. Adapt from Ref.[10].

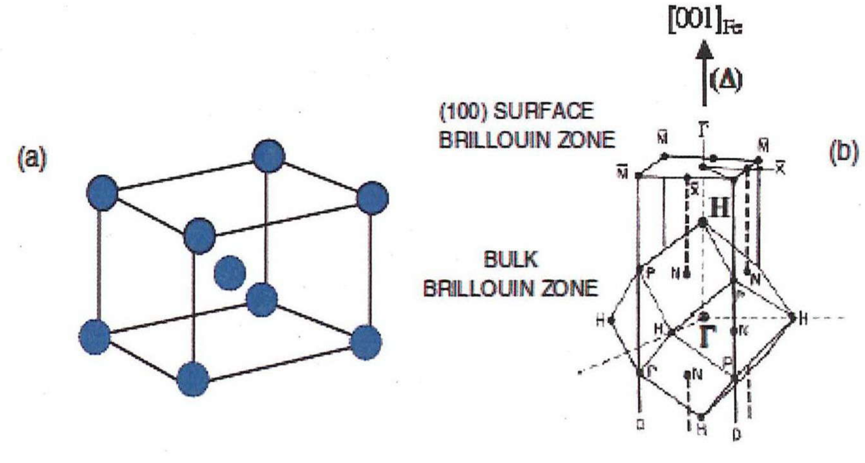

**Fig. 1.3**

Schematic illustrations of (a) real space and (b) reciprocal space (right) representation of the bcc Fe lattice. For the reciprocal space (Brillouin zone) one can distinguish the high symmetry points and also the specific (Γ–H) direction denoted by Δ. This direction corresponds to the propagation of electrons perpendicular to the Fe(001) plane in real space. The (001) surface Brillouin zone is also represented; one can distinguished the specific direction $\bar{\Gamma}$-$\bar{X}$ where the $k_{\parallel}$ is 0 in $\bar{\Gamma}$. Adapt from Ref. [9].

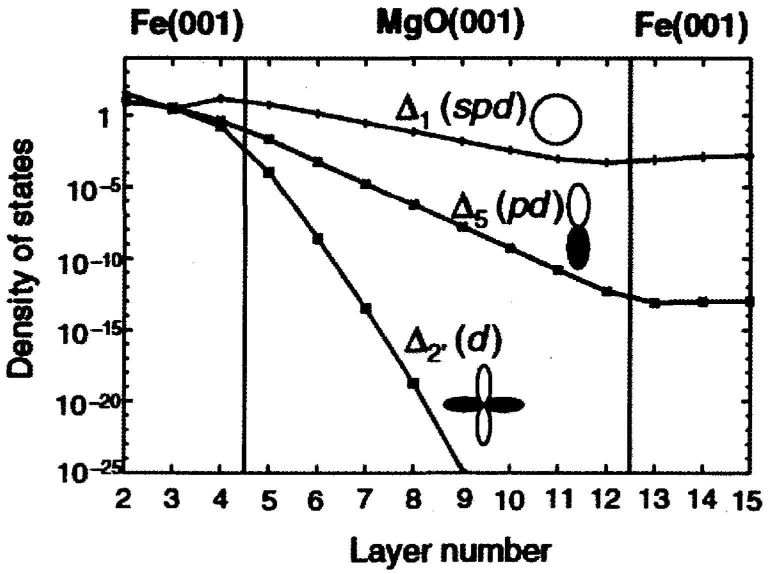

**Fig. 1.4**

Tunneling DOS of majority-spin states for $k_\parallel = 0$ in Fe(001)/MgO(001)(8 ML)/Fe(001) with parallel magnetic state. Adapt from [5] and [10].

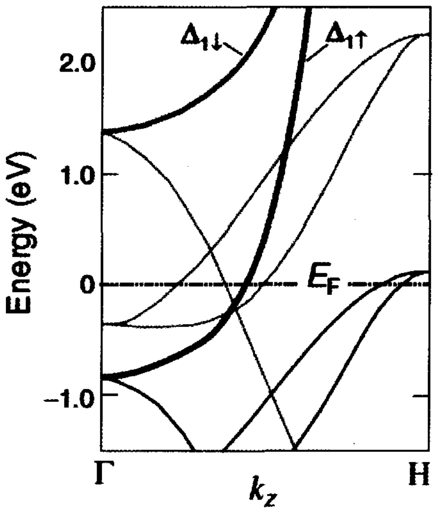

**Fig. 1.5**

Band dispersion of bcc Fe in the [001] (Γ–H) direction. Black and gray lines respectively represent majority- and minority-spin bands. Thick black and gray lines respectively represent majority- and minority-spin $\Delta_1$ bands. $E_F$ denotes Fermi energy. Adapt from [10].

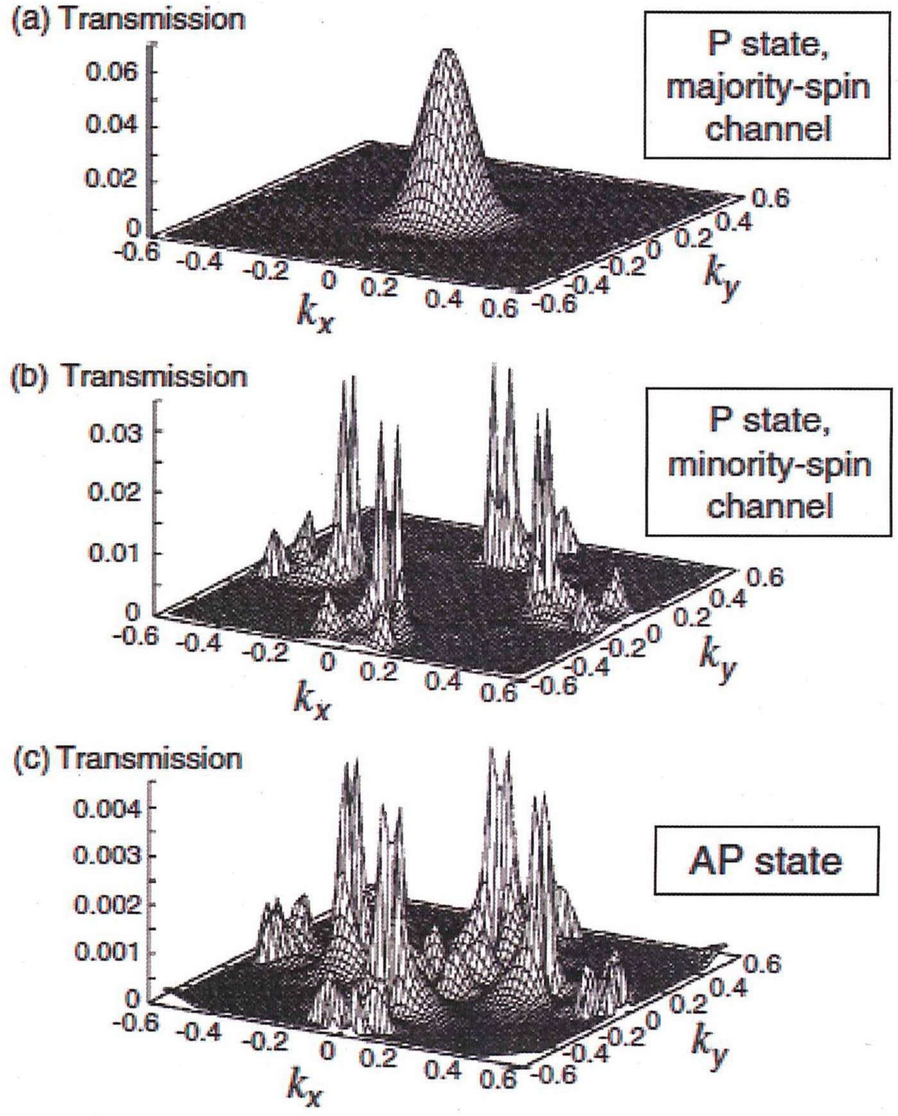

**Fig. 1.6**

Tunneling probability in a Fe(001)/MgO(001)(4 ML)/Fe(001) MTJ as a function of $k_x$ and $k_y$ wave vectors.15) (a) Majority-spin conductance channel in the parallel magnetic state (P state), (b) minority-spin conductance channel in the P state, and (c) conductance channel in the antiparallel magnetic state (AP state). Adapt from Ref. [5].

## 1.3. Quantum Well Effect in MTJs

The discovery of the giant tunneling magnetoresistance (TMR) effect in MgO-based magnetic tunnel junctions (MTJs) [7,8,11] has made a huge contribution to the development of magnetic random access memory. In addition to the large TMR effect, the coherent tunneling property of these junctions is useful for investigation of the fundamental physics of the spin-dependent tunneling effect. On the other hand, electron confinement in quantum wells (QWs) has been extensively studied in semiconductor and metallic heterostructures. It has proven to be a powerful approach to tuning the electronic structure and to tailoring new functionalities in devices such as interlayer exchange coupling between ferromagnets. Quantum confinement of spin polarized electrons or spin-dependent quantum well effects is therefore of great interest for both fundamental and applied spintronics. Up to now, QW effects have successfully been observed in epitaxial MTJ systems by making one of the electrodes very thin to introduce quantum well states [12–19]. The most intriguing aspect expected in this structure is an enhancement of the TMR effect due to the resonant tunneling effect through the QW states [20]. Generally there are several kinds structures have been used for QW states in MTJs.

(I) One of the two FM electrodes is made of an ultrathin single-crystal FM layer the majority spin electrons would be confined in the ultrathin FM layer. If the coherence of the electron wave functions is conserved, the electrons can form spin-polarized quantum-well (QW) states, and the TMR effect can be modulated by the QW states. For example in the Cr(001)/ultrathin Fe(001)/insulator/Fe(Co) structure [12,16,17,19,20]. This QW states arises from the band mismatch between Fe and Cr. T. Nagahama et al. observed the quantum well effect in MTJs with the structure of the Cr(100) (20 nm)/Fe(100) (nML)/Al–O (1.7 nm)/FeCo (20 nm) at 2 K [12]. F. Greullet et al., T. Niizeki et al. and D.Bang observed the quantum well effect in Cr/Fe/MgO/Fe structures at low and room temperature [16,17,19]. Z.Y. Lu et al. did the theoretical calculation work in such structure and presented the quantum resonant energy position for different Fe thickness [20]. However, there is discrepancy in the experiment results and theoretical calculation.

(II) An ultrathin non-magnetic (NM) layer is inserted between the tunnel barrier and one of the FM electrodes, the minority spin electrons are confined in the NM layer and form spin-polarized QW states. For example, in 2002 Yuasa *et al.* have successfully observed QW phenomenon in the Co(001)/ultrathin Cu(001)/Al-O/Ni-Fe structure, where TMR ratio oscillates with NM thickness due to the change of the discrete energy level states in the QW [13]. And then in 2004, Nozaki *et al.* found QW states formed in a Ru spacer layer in $Co_{90}Fe_{10}$(1.2)/Ru(t)/Al (1.1)-$O_x$/$Co_{90}Fe_{10}$ (3)/Ta(3) (the numbers are film thickness in nm) MTJs and also investigated the influence of QW states on TMR [21].

(III) An ultrathin FM layer is sandwiched by two tunnel barrier layers forms double barrier MTJs. For example, in 2006, T. Nozaki *et al* found resonant tunneling effects in macroscopic DMTJs (MgO seed layer(10nm)/Fe(50nm)/MgO(2nm)/Fe(t)/MgO(2nm)/Fe(15nm)with Fe nanoislands incorporated into the thick MgO barrier, which can be explained by the combined QWS and coulomb blockade effects [14]. In 2008, Iovan *et al.* gave evidence for a local tunneling through QWS in the central Fe layer in F1/I1/F2/I2/N samples of structure Si/SiO/Fe(50 nm)/MgO(3 nm)/Fe(1–2 nm)/MgO(2–3 nm)/Au(30 nm) using the point contact technique. Those experiment results were also in accordance with Y. Wang et al. theoretical calculation result [15,18].

## 1.4. Quantum Well Effect in MTJs with Cr/ Ultra-thin Fe/MgO/Fe Structure

More detail research progress for quantum well effect in Cr/ ultra-thin Fe/MgO/Fe MTJs is discussed here, since the author's main work based on this structure.

The advantage of MTJs with single-crystal Fe/MgO/Fe structure has been interpreted in Sec. 1.3. Due to the coherent tunneling process in Fe and MgO barrier, high MR ratio was obtained. Electrons with $\Delta_1$ symmetry electrons wave functions play an important role in such process. On the other hand, Cr as an very important materials is frequently been used in spintronics research because of its special characteristics of magnetic structure and band structure.

As the magnetic structure characteristics of Cr(001), it shows a layered antiferromagnetic (LAF) structure. The magnetic moments of Cr(001) are ferromagnetically aligned within each monatomic layer, and the magnetizations of each atomic layer are aligned opposite to the magnetizations of the adjacent layers, so GMR in Fe/Cr/Fe multilayers can be observed, which is recognized as milestone in spintronics research. A.Fert and mo also received the Nobel prize for their fist founding of that. The band structure of bulk Cr along the (001) direction calculated by the layer-Korringa-Kohn- Rostoker (KKR) method is shown in Fig. 1.7 (b). Because of the mismatch of $\Delta_1$ band structure at $E_F$ in Fe and Cr, quantum well effect can be expected. See Fig.1.7. There is no $\Delta_1$ band (s band) around the $E_F$. In the MTJs without a $\Delta_1$ band (s band), the electrons are reflected at the Fe/Cr interface, because there are no states (i.e., no $\Delta_1$ band) available for coherent tunneling.

So far F. Greullet *et al*, and T. Niizeki *et al* have observed quantum well effect experimentally in Cr/Fe/MgO/Fe MTJs [16], which were deposited by MEB and sputtering respectively. F. Greullet *et al* observed small oscillation from $dI/dV$ spectrum and more clear oscillation from $d^2I/dV^2$, see Fig.1.8. After their work, T. Niizeki *et al* observed more clear oscillation in $dI/dV$ spectrum, see in Fig.1.9. What's more important, similar with a map of QW states shown in Ref. 22 (see Fig. 1.10), in the case of a Cu QW observed by photoemission, they also presented the resonant peak position with the change of Fe thickness and applied voltage, see Fig 1.11. The periodical peak to dip of $dI/dV$ values were observed, which indicated the quantum interference modulation characters.

More precise and quantitative discussion is still needed in this research. T. Niizeki *et al* demonstrated good agreement from their experiment data with Z.Y. Lu *et al* calculation, which assumed 1ML FeO at Fe/MgO interface. However, both of them didn't have direct evidence for the formation of FeO at Fe/MgO interface. In addition, no one presented the data of $dI/dV$ for continues thickness of Fe, just show the integer thickness data can not convince people the change of $dI/dV$ values were modulated by quantum effect. More detail investigation is still needed for deep understanding.

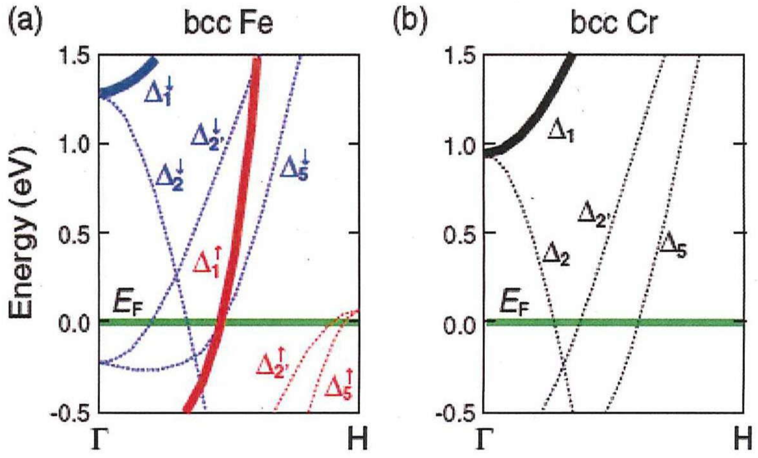

**Fig.1.7**

Band structure in the (001) (Γ–H) direction (a) bcc Fe and (b) bcc Cr. Adapt from Ref.[17].

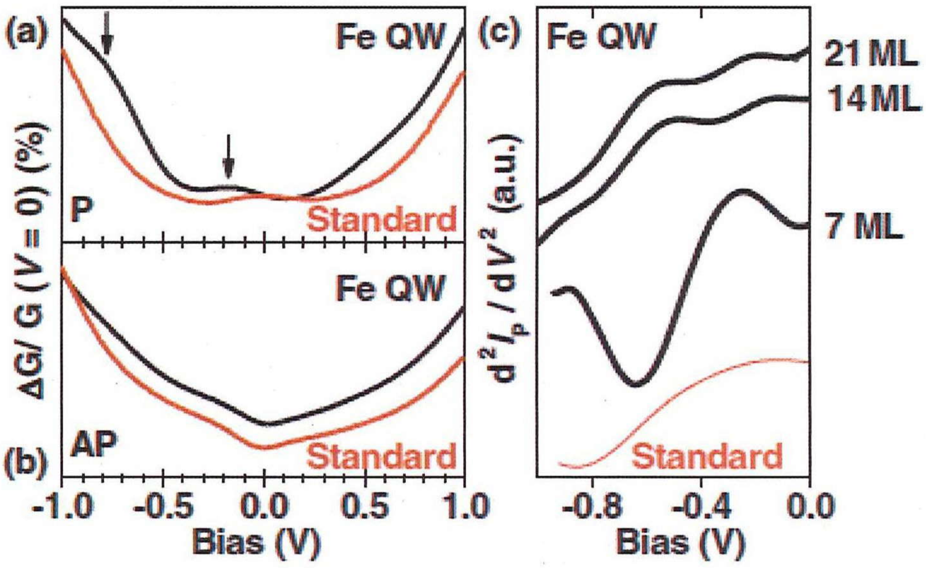

**Fig.1.8**

Relative variation of $G_{P(AP)}(V)$ in standard Fe/MgO/Fe and Fe (7 ML) QW MTJs in the (a) P and (b) AP junction states. (c) $d^2I_P/V^2(V)$ data for Fe/MgO/Fe and Fe($d$) QW MTJs. Adapt from Ref.[16].

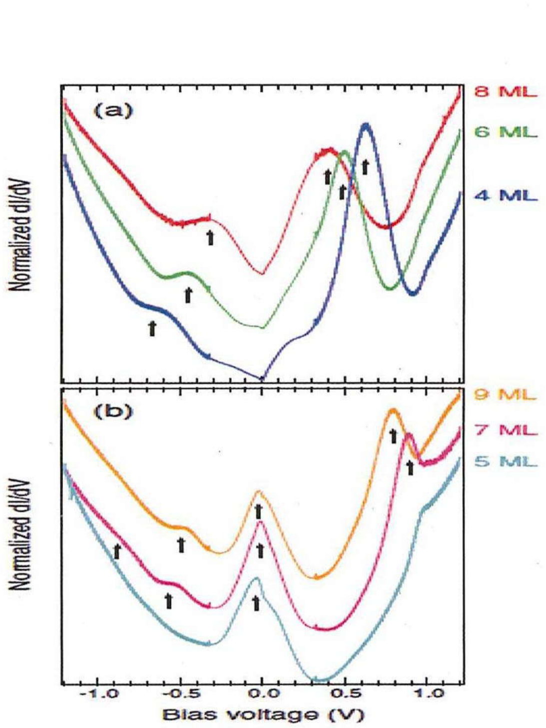

**Fig.1.9**

(a),(b) The differential conductance (*dI/dV*) spectra in the parallel magnetization configuration for (a) d = 4, 6, 8 ML and (b) 5, 7, 9 ML. Adapt from Ref.[17].

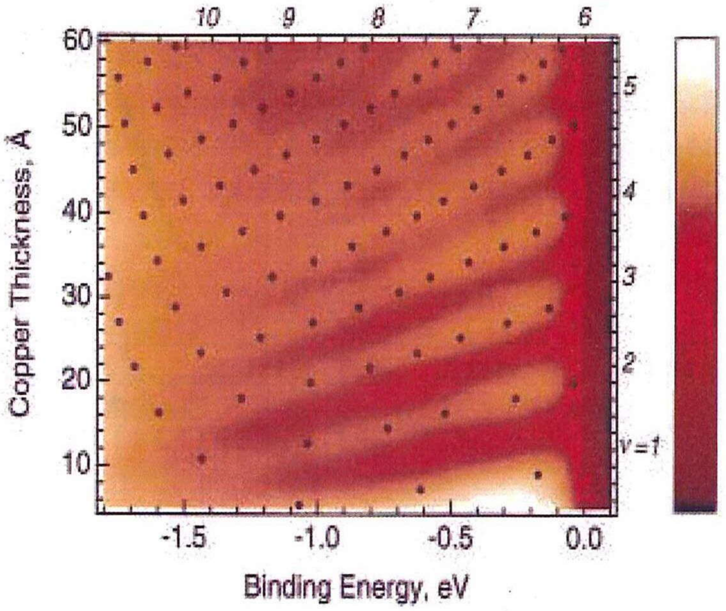

**Fig.1.10**

Experimental results (color image) of the Cu quantum well states in the Cu/Co(100) system and the theoretical calculation (filled circles) using the phase accumulation method. The color key is on a linear scale. Adapt from Ref. [22].

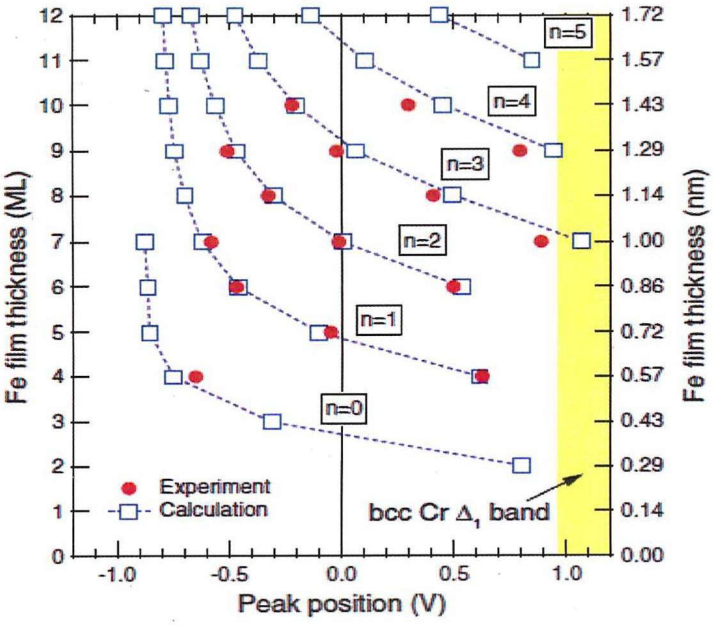

**Fig.1.11**

Ultrathin Fe(001) layer thickness versus the resonant peak positions. The circles and the squares represent the experimental data and the *ab* initio calculations [20], respectively.
The dashed lines categorize the squares by the node number (n) of the standing wave created in the ultrathin Fe(001). Adapt from Ref. [17].

## 1.5. Interface status of Fe/MgO and Cr/Fe

In this sections the author presents the results of experimental and theoretical investigations of the crystallographic and chemical profiles at the interface of between the epitaxial Fe(001) bottom electrode and the MgO barrier in Fe/MgO/Fe MTJs and interface between Cr buffer and Fe(001) bottom electrode.

### 1.5.1 Fe/MgO interface (MgO growth on Fe)

In Fe/MgO/Fe MTJs, the interface status is an issue of universal concern, since its effect on TMR ratio. Extensive investigations were performed by many researchers. Even now for the case: interface between the Fe(001) bottom electrode and the MgO barrier, is still a controversial problem. Here the author would like to review the Fe/MgO interface experimental research results so far.

In 2001 Meyerheim *et al.* presented the first experimental evidence of an FeO layer between bottom Fe(001) and MgO barrier, using surface X-ray diffraction [23]. They built their model of the bottom oxidized Fe interface, with concerning interlayer distances. And then in 2003, first-principles calculation of the electronic structure and MR ratio of Fe/FeO/MgO/Fe tunneling junctions with FeO layer at the bottom Fe/MgO interface was done by Zhang *et al.*, with a detailed comparison to those of pure Fe/MgO/Fe junctions [24, 25]. They argued that an atomic layer of FeO at the Fe/MgO interface immensely reduces the TMR ratio, because the in-plane bonding of Fe with O reduces the conductance in the P state, but it has nearly no influence on the AP state conductance. What's more, the TMR ratio decreases monotonically and exponentially with the increasing O concentration in the FeO layer. Theoretical results [24] of first-principles DOS calculations for the ideal interface and the oxidized interface are shown in Fig.1.12. With respect to an ideal interface shown on the left of Fig.1.10, $\Delta_1$ Bloch states in the Fe layer couple with $\Delta_1$ evanescent states in the MgO barrier in the $k_{\parallel} = 0$ direction. This structure with an ideal interface presents a very large MR ratio [5]. For an oxidized interface shown on the right of Fig.1.12, where there are excess oxygen atoms in the interfacial Fe monolayer. Since $\Delta_1$ Bloch states in the Fe layer do not couple with $\Delta_1$ evanescent states in the MgO barrier effectively, such decoupling shows coherent tunneling of $\Delta_1$ states and greatly reduces the MR ratio [26].

After that, more and more analytical techniques have been employed to investigate the interface characterization of MgO-based epitaxial MTJs, such as Auger electron spectroscopy (AES), X-ray absorption spectra (XAS), and X-ray magnetic circular dichroism (XMCD).

In 2003, H. Oh and S. B. Lee *et al.* investigated the chemical structure of the interface formed during the growth process of MgO deposit on Fe (001) by vibration spectroscopy employing a high resolution electron energy loss spectrometer [27]. They found direct, spectroscopic evidence for the formation of FeO layer at the interface that is triggered by the dissociation of oxygen molecule by deposited Mg. They concluded that FeO cannot be eradicated at the interface at Fe/MgO. However, their MgO deposition method is that MgO was deposited by reactive oxidation: Mg was thermally evaporated in a chamber backfilled with oxygen molecules whose partial pressure was $2 \times 10^{-8}$ Torr.

And then in 2005, F. J. Palomares and C. Munuera *et al.* studied the chemical nature of the different interfaces and possible segregation effects in fully epitaxial Fe/MgO/Fe (001) oriented heterostructures by AES measurement [28]. Their Auger electron spectroscopy depth profiling experiments suggested that the interfaces of the MgO spacer with the Fe layers are different. They concluded that the FeO was formed between bottom Fe(001) electrode and MgO barrier interface, but no evidence of FeO formation at between MgO barrier and top Fe electrode. They attributed such spatial and chemical asymmetry to the different deposition procedures, which affect the formation of both interfaces. They also declare that Fe segregation in the MgO layers or MgO segregation in the Fe films is not observed. In their experiment, the sample was fabricated by combined sputtering plus laser ablation deposition techniques.

On the other hand, in 2003, M. Sicot, M. Andrieu, and P. Turban *et al.* investigated the interface of 6 monolayer (ML) Fe(001) in Fe/MgO bilayers by XAS and XMCD [29], their results demonstrated that there is a weak hybridization between Fe and O atoms but no evidence for Fe oxidation. In 2005, K. Miyokawa *et al.* provided the evidence for a free Fe oxidization interface by the XAS and XMCD measurements, which is performed on 1 ML and 2 ML-Fe(001) facing an MgO(001) barrier with (bcc) Co(001)/Fe(001)/MgO(001) structure [30], see in Fig.1.13. Since the limitation of measurement techniques, in these above experiments no complete MTJs were fabricated, TMR ratio data were absent, which should also gave evidence for the possible formation of an FeO monolayer.

In 2007, M. Müller, F. Matthes, and C. M. Schneider symmetrically investigated electronic structure study of the MgO/Fe(001) system with ultrathin MgO layers using spin-resolved photoelectron spectroscopy [31]. They deposited Fe(001) films by electron beam evaporation with the substrate held at 400 K. In a following step, ultrathin MgO overlayers of about 1 ML thickness were grown by depositing metallic Mg in an oxygen backpressure. The Mg level of oxidation was controlled by offering variable oxygen exposures during growth. They conducted different oxidation procedures, and found that deposition of Mg with increased oxygen amount supply resulted in different interface types: Fe/Mg/MgO, Fe/MgO and Fe/FeO/MgO respectively.

Recently, D. Telesca *et al.* performed X-ray absorption spectroscopy and X-ray scattering measurement to determine the oxidation reactions at the buried MgO/Fe interface as a result of the deposition of MgO [32]. They confirmed that less than 1 ML in thickness Fe-oxide was present at the MgO/Fe and MgO/CoFe interfaces. Their samples were prepared by sputter deposition using a combination of ion-beam and magnetron sputtering at room temperature in precisely the same way as the MTJ samples reported earlier.

What is worth mentioning, P.J. Zermatten *et al.* performed systematic electrical measurements on sets of two MTJs with and without a p(1× 1)-O monolayer at the Fe/MgO interface. The FeO interfacial layer was obtained by introducing molecular oxygen through a leak valve and adsorbed at RT on the free Fe(001) surface of sample. The adsorbed amount was controlled in real time by X-ray photoelectron spectroscopy (XPS), so they could stop the deposition immediately after the adsorption of one oxygen monolayer. Subsequent annealing is performed at 925K (both samples were annealed) resulted in the p(1× 1) ordering of the oxygen overlayer. In agreement with theory, the FeO layer reduces the conductance in the P configuration by one order of magnitude, equivalently to the addition of two MgO layers. In addition, their study showed that the presence of interfacial FeO can be inferred from the value of the RA (Resistance and MTJ Area) product. Based on their result, there is no Fe oxide at the Fe/MgO interface when MgO is growth on Fe without intentional oxygen absorption [33].

In short, so far people still not reach consistent conclusion about the extent of Fe/MgO interface oxidation for MgO growth on Fe buffer. However, it is clear that the presence of Fe oxide or not at Fe/MgO interface depends on the deposition condition. The author believes that epitaxial deposition of Fe and MgO by electron beam evaporation at room temperature, Fe oxidization can be avoided. The author will discuss this point in the later part of this thesis.

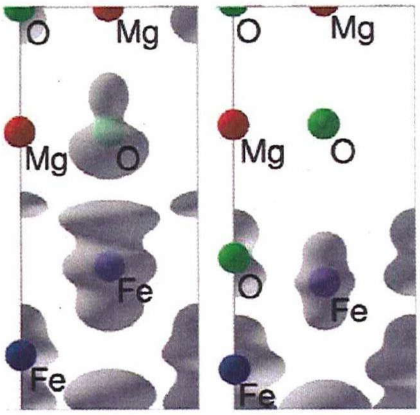

**Fig. 1.12**

The partial density of states at the Fermi energy due to the $\Delta_1$ state in the majority spin channel near the interface region. Left panel, without the FeO layer; right panel, with the FeO layer. Adapt from Ref. [24].

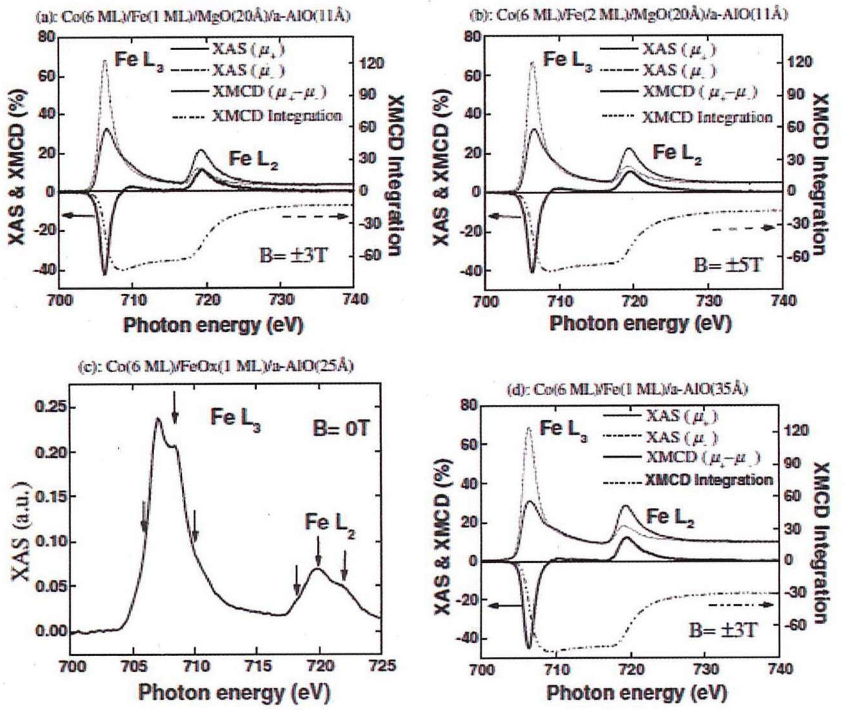

**Fig. 1.13**

X-ray absorption spectra (XAS) and X-ray magnetic circular dichroism (XMCD) spectra at Fe-$L_{2,3}$ edges in samples (a), (b) and (d). The XAS spectra of these samples were measured at magnetic fields (***B***) of ±3 T, ±3 T and ±5 T, respectively. The XAS spectra of sample (c) was measured at ***B*** =0 T. Adapt from Ref. [30].

### 1.5.2 Cr/Fe interface (Fe growth on Cr)

As the interface research between Fe(001)/Cr(001), exchange coupling at the interface between ferromagnetic (FM) and antiferromagnetic (AF) materials, such as Fe/Cr(001) sandwiches and superlattices have attracted much attention not only from a practical application to spin-electronic devices but also from a physical point of view, because they present giant magnetoresistance (GMR). People found that AF–FM interfaces are not always ideal and the microscopic interface structure plays a crucial role in exchange coupling. It is important to have a better understanding of the interface formation and of its electronic structure.

Generally, the interface status for Fe(001) deposited on Cr(001) is different from the case of Cr(001) deposit on Fe(001). Since the author's work is related with Fe(001) deposit on Cr(001) buffer, here the author will only review the research of interface between Cr(001) buffer layer and Fe(001).

In order to gain further insight into it, detailed information on surface and interface structures including chemical analyses is important for understanding these mechanisms. Microscopic investigation of the growth of Fe films on Cr(001) by using scanning tunneling microscopy (STM) is a powerful way to research such problem.

In 1999, Y. J. Choi *et al.* observed surface alloy formation of Fe on a Cr(001) surface by a UHV scanning tunneling microscope [34]. When they deposited Fe of less than 1 ML at room temperature and subsequently annealed the substrate at temperatures between 200 °C and 300 °C, they found that Fe atoms incorporate into the Cr(001) surface, forming a well-ordered surface alloy of $Fe_{0.5}Cr_{0.5}$. Incorporated Fe atoms are identified by the difference in tunneling currents at the bias voltage of the Cr surface state and at that of the Fe surface state. The alloyed area can also be differentiated by measuring the change of the work function at the alloyed region from that at a bare Cr surface. Since Fe has a localized surface state just above the Fermi level and Cr has one just below the Fermi level, one can distinguish Fe atoms from the Cr substrate if the tunneling voltage is set at the Fe surface state. Beside the alloy formation at the low Fe coverage, they also concluded that layer-by-layer growth of Fe layers can be achieved at the Fe coverage of ~1 ML by annealing the sample at 250 °C, see Fig.1.14 and Fig.1.15.

In 2003, R. Ravlić,M. Bode and R. Wiesendanger studied the growth of Fe on Cr(001) as well as the dependence of the electronic and magnetic structure on the Fe coverage by spin-polarized scanning tunneling microscopy [35]. Their results revealed an almost perfect layer-by-layer growth for $\theta \leq 1.48$ML and for $\theta \geq 3$ML. In the intermediate coverage range (1.48ML< $\theta$ < 3 ML) the simultaneous growth of second and third ML islands is observed. Fig. 1.16 shows the typical tunnelling spectrum of the c(2× 2)-ordered Fe/Cr alloy as a reference. What is worthy of note, they found the Fe films on Cr(001) are unstable against intermixing even at RT. This is shown by time-dependent topological and electronic structure investigations (see Fig.1.17). In 2006, Takeshi KAWAGOE *et al.* presented the growth and tunneling d*I*/d*V* spectra of ultrathin Fe films (0.5 < Fe < 2ML) on Cr(001) substrates, together with the magnetic imaging of the Cr(001) film, by STM combined with spectroscopy. They have never observed a double-peaked d*I*/d*V* spectrum, as observed for the Cr–Fe ordered alloy, see Fig 1.1.18 (a) and (b). These results indicate that the ultrathin 2ML Fe(001) film is not subjected to appreciable intermixing or alloying with Cr just after annealing at 300°C. They concluded that the RT growth and postannealing at 300 °C of 2ML Fe films on this Cr(001) film provide atomically flat and chemically clean surfaces and the first Fe layer is most likely affected by the intermixing with the Cr atom [36].

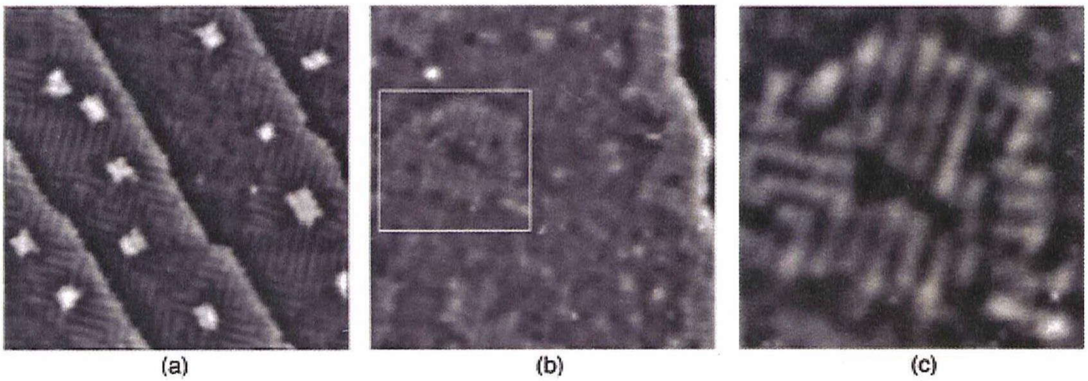

**Fig. 1.14**

Surface alloy by incorporation Fe atoms into Cr matrix. There can be seen the Fe atomic rows, which are brighter than Cr bare terraces and darker than Fe islands with 1-ML height. The incorporation of Fe atoms started from island or step edges. When the annealing temperature is 300 °C, the alloyed area was found on the terrace. (a) $T$=200 °C, (b) $T$=300 °C, (c) close-up view of the alloyed area in (b). All the images were taken at the Fe surface state ($V_s$=0.3 V) and the image sizes are 180 × 180 Å except (c). Additional black and white lines appear along the step edges in the process of enhancing the image contrast. Adapt from Ref. [34].

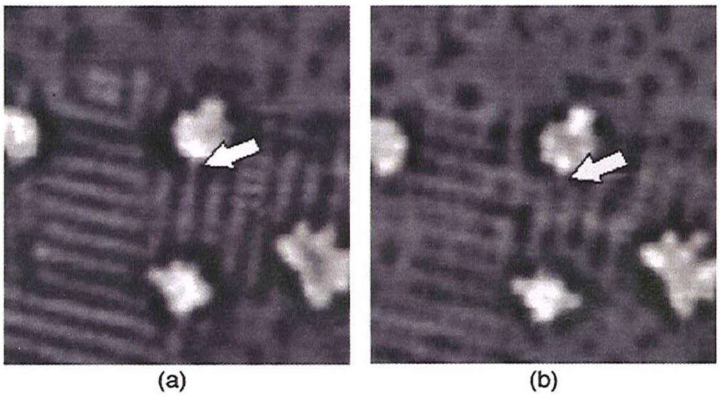

**Fig. 1.15**

Identification of different elements in the alloyed regions using surface states. (a) $V_s$=0.3 V (Fe surface state), (b) $V_s$=-0.2 V (Cr surface state). The contrast of the atomic row marked by an arrow is reversed as the sample bias is changed from 0.3 to -0.2 V. The image sizes are 80×90 Å and $T$=200 °C. Adapt from Ref. [34].

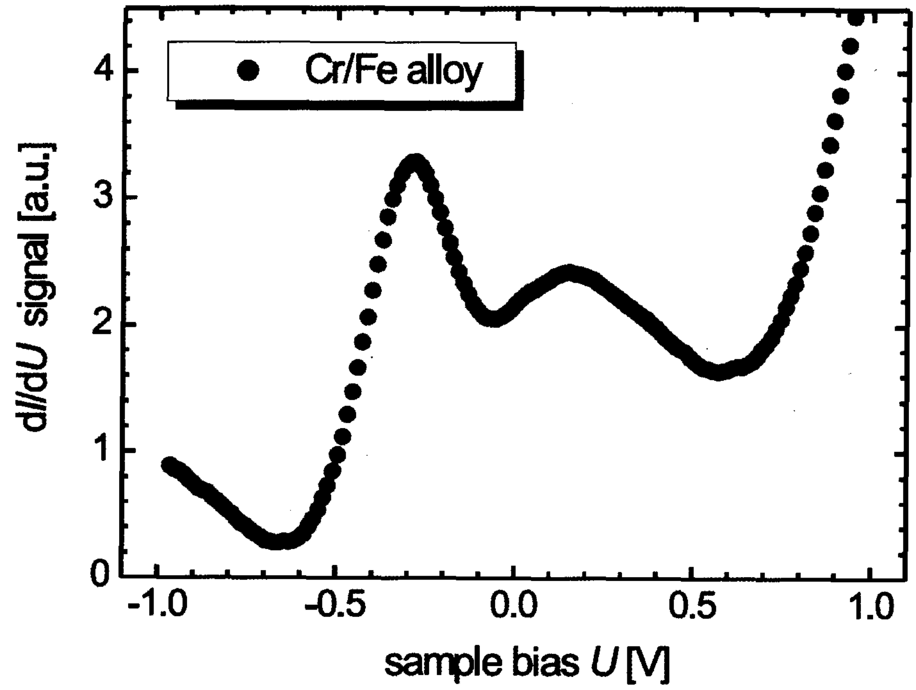

**Fig. 1.16**

Typical tunnelling spectrum of the c(2× 2)-ordered Fe/Cr alloy with its characteristic double peak structure. Adapt from Ref. [35].

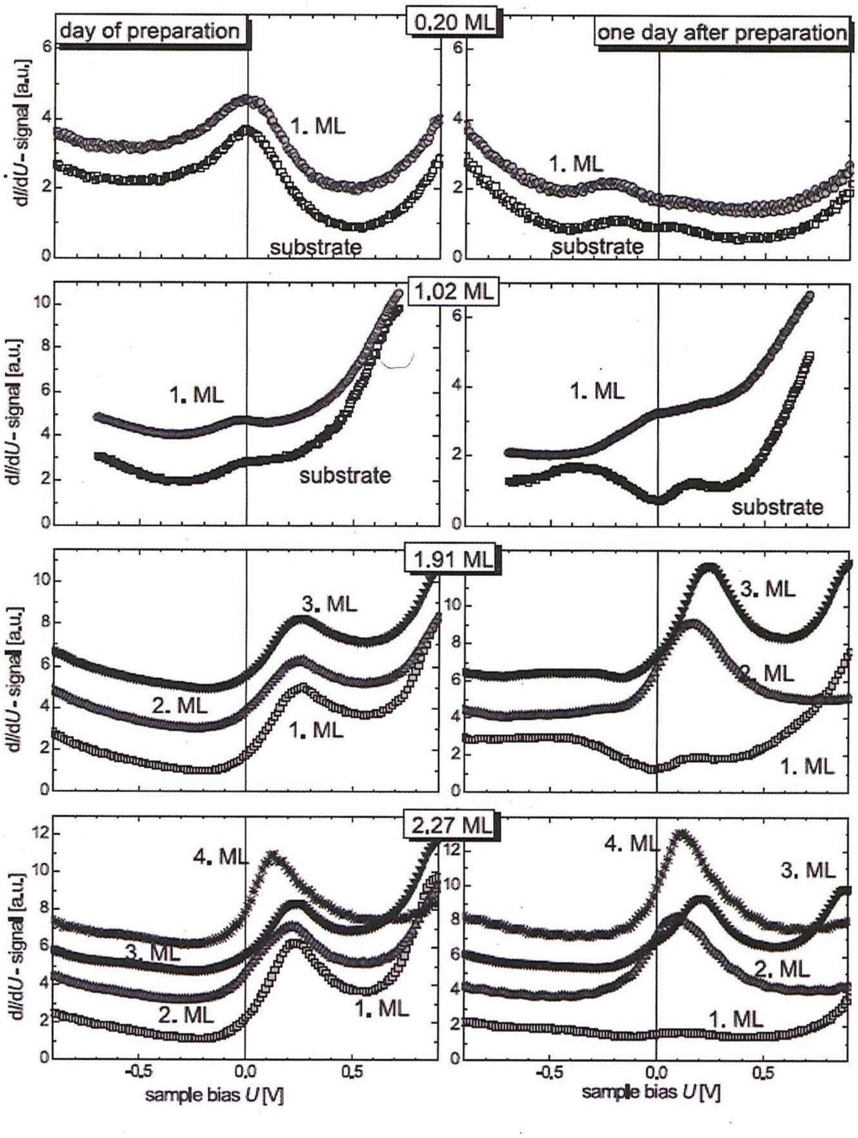

**Fig.1.17**

Thickness-dependent electronic structure of Fe films on Cr(001) shortly after (left column) and one day after preparation of the sample (right column) as measured by STS using a non-magnetic W tip. For better visibility different STS curves have been shifted by a constant offset relative to each other. At low coverage ($\theta \leq 1.2$ML) the electronic structure of the substrate and the first ML are similar to that of the clean Cr(001) substrate, i.e. with a single peak at EF. At higher coverage ($\theta \geq 1.9$ML) the peak shifts to U ≈ +0.2 V. One day after preparation the d*I*/d*U* spectra of layers closest to the Fe/Cr interface have changed. Now, a double peak structure being characteristic for an ordered Fe/Cr alloy is visible. Adapt from Ref. [35].

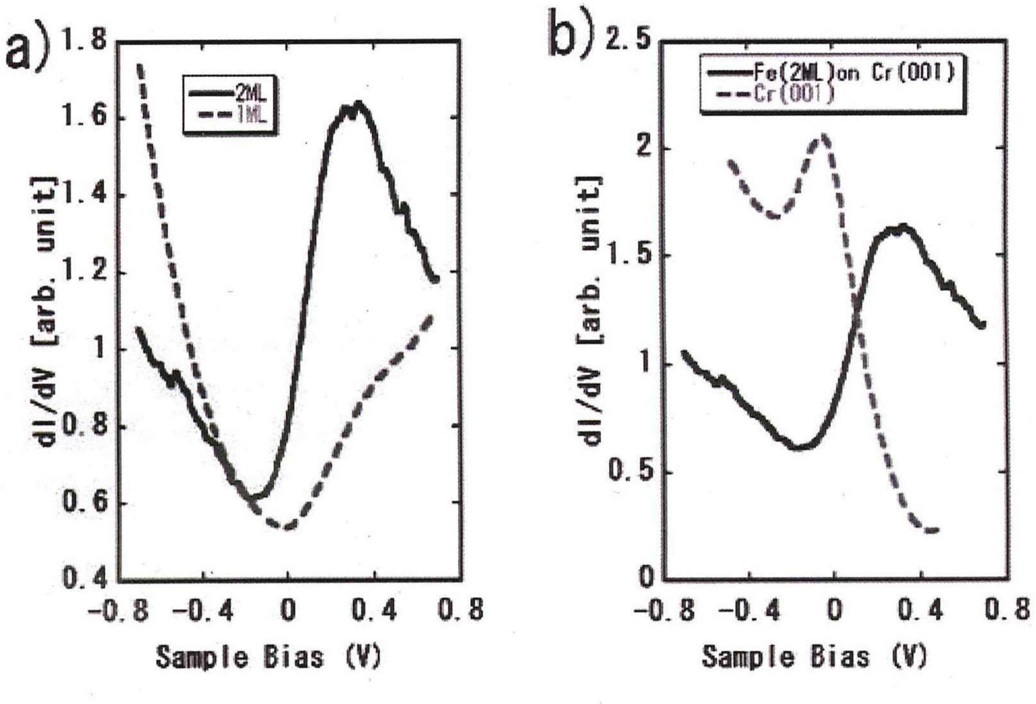

**Fig. 1.18**

(a) Average d*I*/d*V* spectra of ultrathin Fe films on Cr(001) for Fe =1ML with $T_{pa}$= 200 °C and Fe = 2ML with $T_{pa}$ =300 °C. (b) Average d*I*/d*V* spectra of Cr(001) film and ultrathin Fe film (2 ML) with $T_{pa}$ = 300 °C on Cr(001) film. Adapt from Ref. [36].

# CHAPTER 2 EXPERIMENT METHOD

The author's experiments were performed in Prof. Yoshishige. SUZUKI laboratory, Graduate School of Engineering Science, Osaka University, except the X-ray absorption spectroscopy and magnetic circular dichroism measurements were conducted on beamline BL25SU at SPring-8 synchrotron.

## 2.1 Thin film deposition and thickness calibration

The author deposited all of the epitaxial MTJs films and other multilayer junction films by molecular beam epitaxy (MBE) method.

### 2.1.1 Thin film deposition process

Cleaning process: a single crystal MgO(001) substrate was cleaned by acetone and 2-propanol solvents in ultrasonic washing bath to remove the contaminants. And then, it was degassed at 600°C for around 45minutes in the MBE introduce chamber with high vacuum (base pressure ~$10^{-7}$ Pa) which connect with the growth chamber of MBE to remove the adsorbed impurity atoms and molecules.

Deposition process for MTJs: Fully epitaxial MTJs consisting of Cr(001) (40 nm)/wedge shaped ultrathin Fe(001) (0–12 ML)/MgO(001) barrier/top Fe(001) (4 nm) were grown on MgO(001) substrates with a base pressure of $6\times10^{-8}$ Pa (see Fig. 2.1).

At first, 10nm MgO seed layer was deposited and then annealed at around 200 ~300 °C to improve the morphology of the substrate surface. After that, 40nm Cr was deposited at room temperature and then annealed at ~350 °C for 30 minutes and then cool down to room temperature to obtain very flat surface. Next step, the ultrathin Fe wedge layer was deposited at room temperature. It was grown by moving a rectangular shutter linearly with constant speed. One of the quadrate substrate edges was adjusted parallel to the shadow of shutter edge before Fe deposition (see Fig.2.2). The ultra thin Fe layer was usually post-annealed at ~250 °C for 20 minutes. The author also investigated the case without annealing. It will be discussed in the next chapter. For the 2nm MgO barrier and top 4nm Fe layers, both were deposited at room temperature annealed at ~250 °C for about 20 minutes. This layer was coupled with Cr/Fe to obtain an antiparallel magnetization configuration. Both of Cr and Fe was deposited at ~200 °C. Such Fe/Cr/Fe is a synthetic antiferromagnet exchange coupling structure with higher coercive force. After all of the above deposition, the sample was annealed at ~250 °C for about 15minutes. In the end, 20nm Au was deposited as cap layer at room temperature.

Deposition process for Cr/ultrathin Fe/MgO junctions for MOKE and XAS and MCD measurement: the deposition process is the same as it use for MTJs, excerpt for XAS and MCD measurement case, the ultrathin Fe was not annealed after deposition.

**Fig. 2.1**

Fully epitaxial MTJs layered structure: consisting of Cr(001) (40 nm)/wedge shaped ultrathin Fe(001) (0–12 ML)/MgO(001) barrier/top Fe(001) (4 nm)

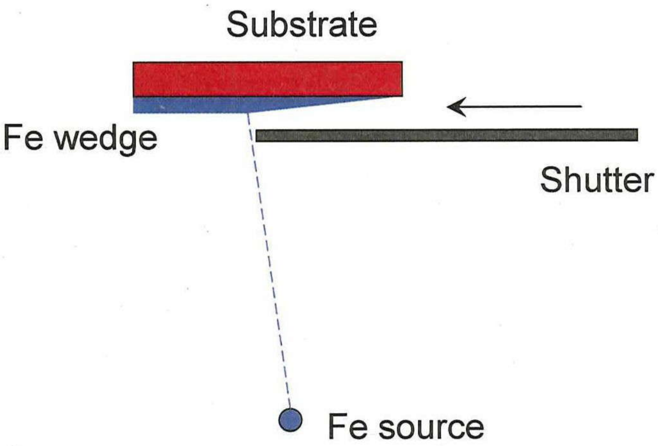

**Fig. 2.2**

Illustration of Fe wedge deposition. The arrow indicates the movement direction of shutter during deposition.

### 2.1.2 Thin film thickness calibration by RHEED

As we know that, RHEED is an extremely popular technique for monitoring the growth of thin films. In particular, RHEED is well suited for use in molecular beam epitaxy, we can observe the deposition process to form high quality, ultrapure thin films under ultrahigh vacuum growth conditions.

The intensities of individual spots on the RHEED pattern fluctuate in a periodic manner since the relative surface coverage of the growing thin film. Fig.2.3 shows an example of the intensity fluctuating at a single RHEED point during our MBE growth. Thickness monitor calibration based on such oscillations of RHEED, high precise of the thickness can be obtained.

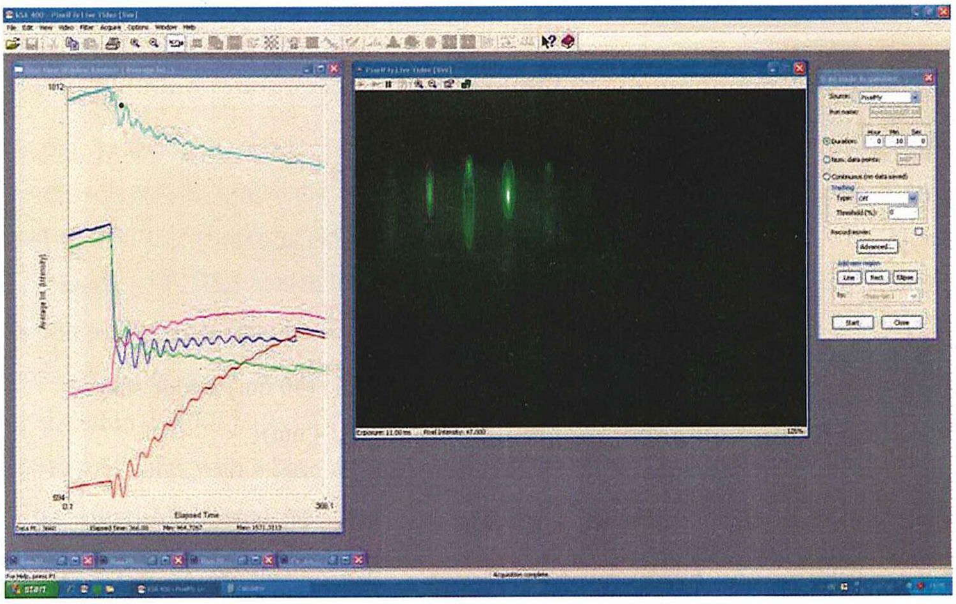

**Fig.2.3**

RHEED Oscillations for Fe at different spots positions.

Different colors indicates different positions.

## 2.2 Sample preparation: Microfabrication

To fabricate MTJs, microfabrication is very important. The design of the MTJs size and pattern location has an effect on our measurement result. In this section, the author presents the details of MTJs moicrofabrication process and the design of them.

After the films were deposited by MBE technique, they were fabricated into tunnel junctions in Osaka University.

Firstly, 150ml TGMR- a kind of the electron-beam negative resist was dropped on the multilayer sample. The sample was spun by spin coater at 1000 rpm and 4000 rpm for 5seconds and 60 seconds respectively. And then it was hardened by baking at 110 °C for 90 seconds. Then by using e-beam lithography, the hardened TGMR covered on sample was exposed. Subsequent post baking was conducted at 120 °C for 90 seconds. After that the resist was developed by NMD-3 to form the designed electrode pattern. In the end, Ar ion milling and lift-off processes were conducted. The films were etched into the bottom MgO buffer layer. Since the TGMR performed as a hard mask, patterned bottom electrode can be obtained.

Secondly, the same processes for MTJ pillars (for example: size1 × 2 $\mu m^2$) as a rectangular matrix of lines which was drawn by e-beam lithography in the TGMR resist, were also performed. The wafer with the hard mask was then etched into MTJ stacks using Ar ion beam milling. The films were etched through from the top Au electrode until to the MgO barrier. The etching depth could be detected by using ion milling probe (IMP-301) based on secondary ion mass spectroscopy system. We could stop etching at the MgO barrier layer, when MgO signal was detected. Then the entire sample surface is covered by a sputtered insulator layer $SiO_2$ of around 9 nm thickness. Lift-off process was conducted to remove $SiO_2$ layer with the TGMR resist and produced contact holes on top of MTJs pillar pattern areas. The MTJs pillar pattern design can be see in Fig.2.4.

Finally, the patterned stacks were capped with Cr(5nm)/Au(60nm) double layers. After the similar process as written above, top electrodes can be obtained. The final structure is a large array with 450 MTJs patterns on each substrate (see Fig. 2.5) after e-beam lithography and Ar ion beam milling.

By using the wedge-shaped ultrathin Fe layer grown on the same substrate, the ultrathin Fe thickness dependences of MTJs conductance could be systematically measured with the negligible error in Fe thickness among MTJs in the same row.

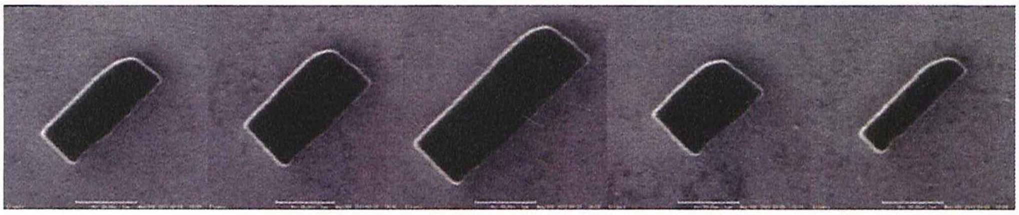
(a) 0.75×2 (b) 1×2 (c) 1×3 (d) 1×1.5 (e) 0.5×2

**Fig. 2.4**

SEM pictures of MTJs pillars with 5 different sizes:
(a)0.75×2, (b)1×2, (c)1×3, (d)1×1.5, (e)0.5×2 with unit in $\mu m^2$.

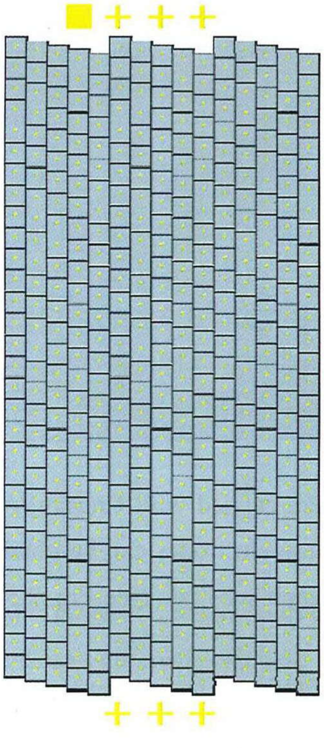

**Fig. 2.5**

Schematic illustration of top view of sample patterns matrix design. The yellow square indicates the MTJ pillar.

## 2.3 Measurement methods

The author's study for quantum well effect and interface status involved dynamic conductance measurement (*dI/dV* measurement), Magneto-optic Kerr effect (MOKE) measurement and XAS and MCD measurements.

***dI/dV* measurement:**

*dI/dV* spectra essentially show a parabolic curve added to a constant conductance. The parabolic increase in dynamic conductance in the high bias region is a consequence of nonlinear conductance in the tunneling junctions [36]. In general, unoccupied states rather than occupied states contribute to the dynamics conductance. Throughout the thesis, the voltage sign is defined with respect to the top electrode, which means that for positive (negative) voltage, electrons tunnel from (to) QW states below (above) the Fermi level. Therefore, in this measurement, since the tunneling electrons flow from the top Fe layer to the bottom Fe ultrathin layer under negative bias, the electronic structure of the ultrathin Fe[100] layer can be effectively observed in the negative bias region (see Fig.2.6). The QW states formed in the ultrathin Fe layer can be indicated by the oscillation of *dI/dV* curve. The details will be discussed in Chapter 3.

We detected *dI/dV* signals with an *I*–*V* converter (OPA627BM operational amplifier), a preamplifier (SEIKO EG&G, Model 5186), and a lock-in amplifier (Stanford Research Systems, Model SR830) (see Fig. 2.6). The *dI/dV* signals were converted as follows:

$$V_{1f} = \frac{dI}{dV} \times R_f \, V_{ac}$$

where the definitions of the ac synchronic signal $V_{1f}$, current I, the dc bias voltage $V$, the ac modulation bias voltage $V_{ac}$ and the resistance $R_f$ are shown in Fig. 2.7.

For our discussion of QW effects, dynamic conductance curves (*dI/dV*) were measured using the conventional lock-in modulation technique at room temperature. The modulation voltage was 1 mV and the frequency was 1.30 kHz.

$$dI/dV \propto (2\pi e^2/\hbar)|t|^2 D_1(E_F)D_2(E_F+eV)$$

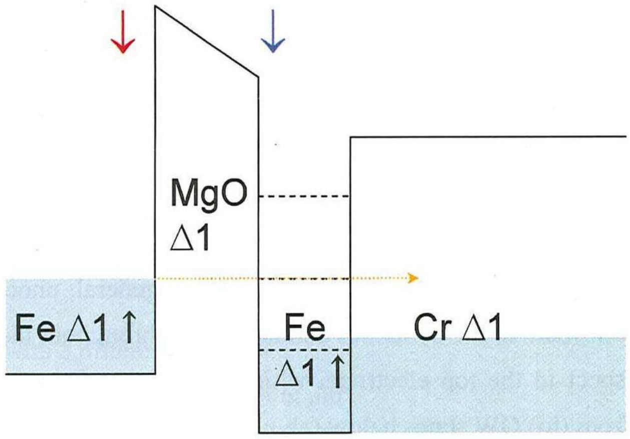

**Fig. 2.6**

Band diagram for Cr/ultrathin Fe/MgO/Fe MTJs. The arrows indicate the DOS of Fe electrode detected corresponding to the *dI/dV* formula.

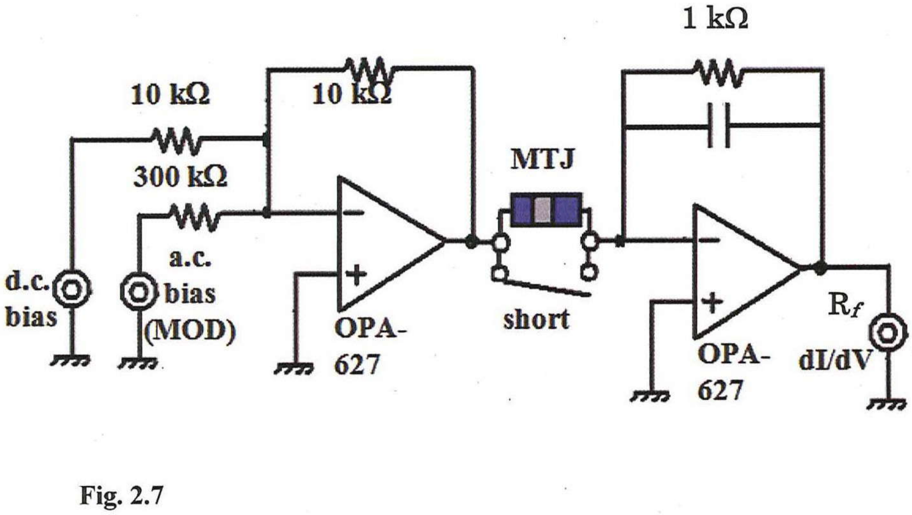

**Fig. 2.7**

Schematic diagram of bridge circuit used for measuring *dI /dV* spectra.

**Magneto-optic Kerr effect (MOKE) measurement** was conducted by the author to study the magnetic property of the ultrathin Fe layer deposited on 40nm Cr(001) buffer. The measurement setup can be seen in Fig. 2.8. The measurement setup includes following parts:

**Laser source**: a Helium Neon Laser was used to generate a light beam.

**Polarizer**: Convert the light of laser source to linear polarization.

**PEM** (Photoelastic Mosulator): PEM is a transparent quartz bar to which is applied a sinusoidal vibration, though a piezo-electric component: an electrical signal is applied to piezoelectric transducers that induces mechanical strain and is transferred to the quartz bar. An input linearly polarized beam becomes elliptically polarized at the output of the modulator.

PEM operates with quarter-wave retardation $\lambda/4$ mode and the frequency of vibration is 42 kHz.

**Lens**: Converging lens is used to focus the laser beam. The elliptically polarized light is concentrated in small area in surface of sample. The reflected light after interacted with magnetic layer of sample can be rotated proportional to magnetization of thin films.

**Analyzer**: Filter the reflected light and achieve the linear polarized light in output. The change of polarization of light is proportional to intensity of light filtered by analyzer.

Photodiode: Change the intensity of light to electric signal.

**Lock-in amplifier**: Electric signal of photodiode is measured by Lock-in technique. The Lock-in amplifier receives the referent signal from sinusoidal vibration of PEM. The electric signal of photodiode has the same frequency with that of PEM and easily to be obtained by Lock-in amplifier with high sensitivity and low noise.

**Electromagnet**: Providing the uniform magnetic field to the sample.

Magnetic hysteresis loops of ultrathin Fe film was measured by using the MOKE in a longitudinal configuration. The voltage dependence of the hysteresis was detected either by a direct observation of Kerr ellipticity, $\eta_K$, signals for different bias voltages, or by a lock-in detection of the small change in Kerr ellipticity with respect to an applied bias voltage modulation, $d\eta_K/dV$. The modulation amplitude and frequency were 160 V (peak-to-peak) and 37 Hz, respectively.

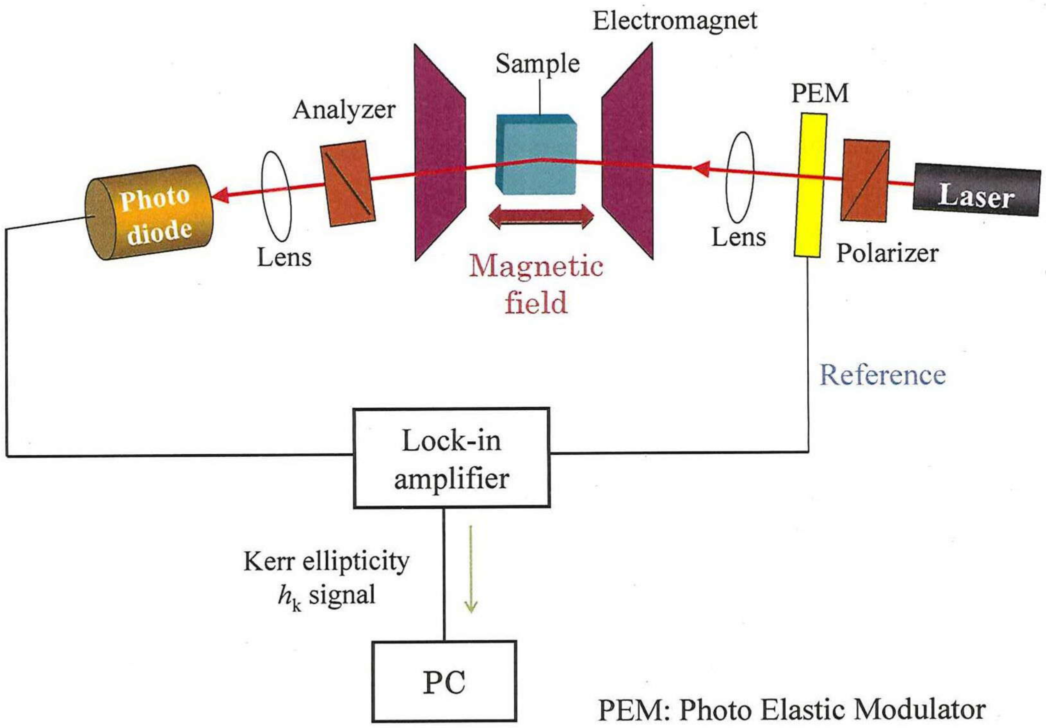

PEM: Photo Elastic Modulator

**Figure 2.8**

MOKE measurement setup with longitudinal configuration diagram.

**XAS and MCD measurements** are a very powerful method to investigate the investigation of exchange anisotropy and other interfacial magnetic phenomena.

**X-ray absorption spectroscopy** is a general name for all X-ray absorption spectroscopy. Common used techniques are XANES (X-ray absorption near edge structure) and EXAFS (Extended X-ray absorption fine structure), which are distinguished by their different energy region. XANES can be applied on determine the oxidation state and coordination, so widely used in transition metal complex study. EXAFS is more sensitive to the local structure of atoms enable it used to determine crystal structure without perfect long-range order. The application of XAS will be related to several fields, especially biochemical, environmental, and catalysis chemistry.

XAS follows the principle of investigating the difference between the intensity of incidence light and transmitted light. As showing in Fig.2.9, when the X-ray interact with a sample, several interaction occurred, including scattering, fluorescence light emission, Auger emission, and transmission. So XAS will have different detection mode by different purposees. In transmission mode, XAS detect the transmitted X-ray, which then can tell the types of atoms due to different absorption edge energies for different atoms. See Fig.2.9.

Suppose the incident intensity of X-rays is $I_0$, the transmitted intensity is I, a fixed thickness of sample is x, XAS will obey an equation: $\ln(I_0/I) = \mu x$, Different types of atoms will give different value of $\mu$.

When the X-ray is "absorbed", what really happened is the radiation knocked the inner electrons out of the atom, which is continuum state, and then gives out as photoelectron. The energies used to overcome different layers of binding energy are absorption edge. The absorption edge is named by the orbital shell the electron coming from. So K edge is the transition that electron was excited from 1*s* orbital, and L edge if electron was excited from 2*s*, 2*p*, M edge if electrons excited from 3*s*, 3*p*, 3*d* as shown in Fig. 2.10.

For light elements, the energy of K edge is not high so usually it is available. But for heavy element, such as many transition metals, especially late transition metals, the energy of K edges are too high to find proper X-ray source. In that case, L or M edges will be used to investigate samples.

**X-ray magnetic circular dichroism** (XMCD) is a difference spectrum of two x-ray absorption spectra (XAS) taken in a magnetic field, one taken with left circularly polarized light, and one with right circularly polarized light. In other word, the circular polarized x-ray is used to measure the difference in absorption. Nowadays, since the development of synchrotron radiation sources, XMCD is a commonly used technique. XMCD is based upon absorption of core electrons with well defined absorption edges. Consequently, the magnetic properties of different element present in the investigated sample can be separated, which is a big advantage compared to techniques that provide information about the average magnetic properties of a sample. Another advantage is that by measuring the difference in x-ray absorption between left and right polarized light and using the so-called sum-rules, it is possible to get separate quantitative information about the spin magnetic moment and the orbital magnetic moment. Due to the mean free path of the electrons, XMCD is a surface sensitive technique.

By closely analyzing the difference in the XMCD spectrum, information can be obtained on the magnetic properties of the atom, such as its spin and orbital magnetic moment.

The magnetic properties of the *3d* transition metals are mainly determined by *d* electrons. Such as the ferromagnets Fe, Co and Ni, the combined 4*s* and 4*p* contribution to the magnetic spin moment is less than 5% and the orbital magnetic moment is entirely due to the *d* electrons. The absorption spectra for XMCD are usually measured at the L-edge. Corresponding to the process in the iron case: with iron, a 2*p* electron is excited to a 3*d* state by an x-ray of about 700 eV. Since the origin of the magnetic properties of the elements are 3*d* electron states, the spectra contain information on the magnetic properties.

The properties of 3*d*-electrons are best probed in an X-ray absorption experiment by excitation of 2*p* core electrons to unfilled 3*d* states as shown in a simple one-electron picture in Fig.2.11. X-rays allow elemental specificity because of the different 2*p* binding energies. There are six sum rules which link polarization dependent p → d X-ray absorption intensities to ground state properties of the d shell. Three sum rules link angle and polarization dependent X-ray absorption intensities to anisotropic d-shell properties: the charge density, the spin density and the angle-dependent orbital moment. Three others allow the determination of angle-integrated d-shell properties: the number of d holes, the magnetic spin moment, and the orbital magnetic moment, see Ref. [38] and reference therein.

XAS/MCD were introduced by the author for the interface research to confirm whether there was $FeO_x$ at the Fe/MgO interface or not. XAS/MCD measurements were performed on beamline BL25SU at SPring-8 synchrotron. The total electron yield absorption spectra was measured under a magnetic field of 1.9 T applied 70° from the surface normal, and with an X-ray incidence of 60°.

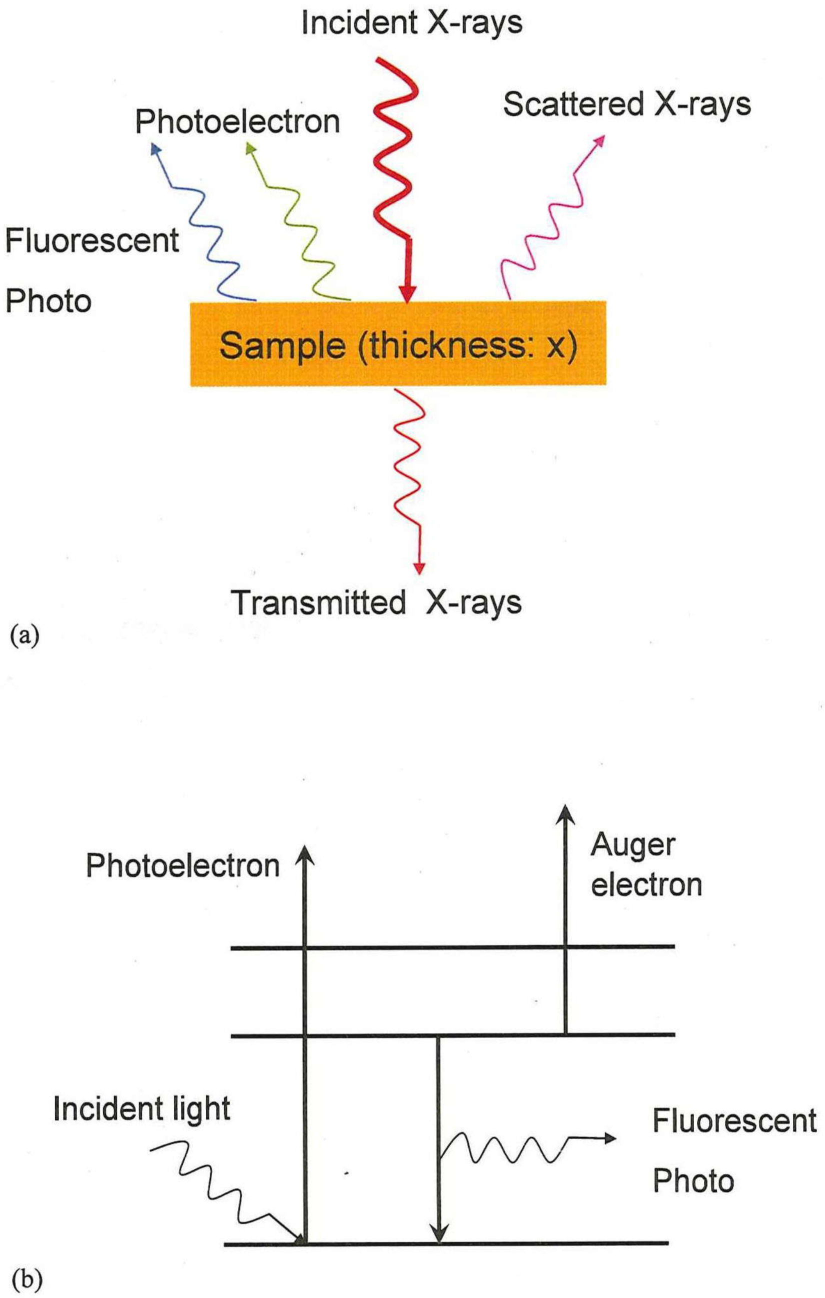

**Fig. 2.9**

(a) Schematic illustration and (b) energy diagram of X-ray absorption process.

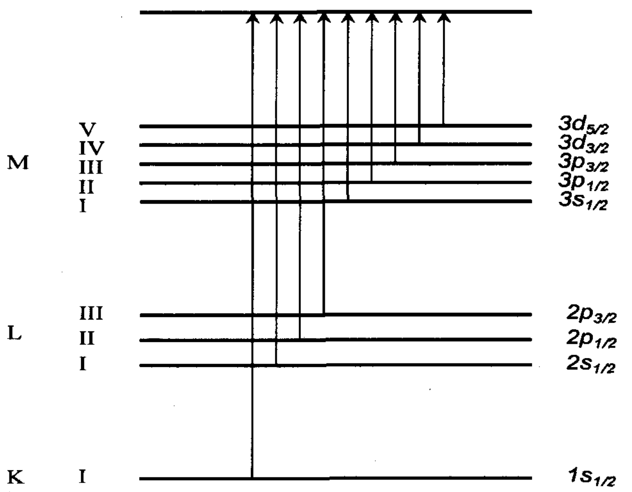

**Fig. 2.10**

Transitions resulting from absorption of X-ray

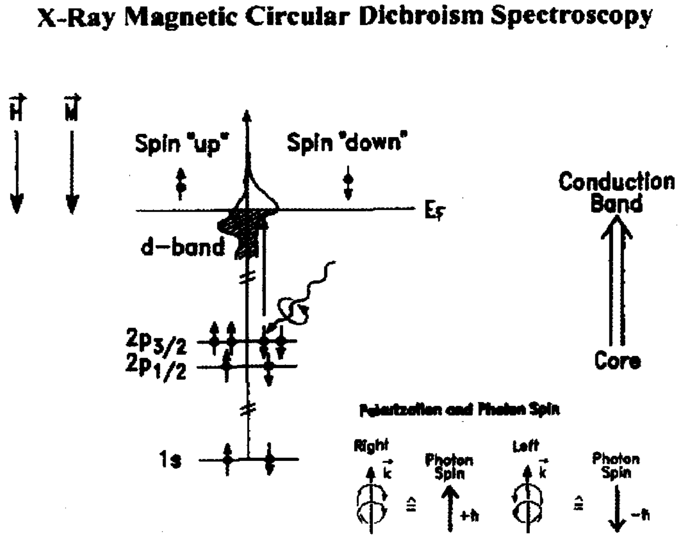

**Fig. 2.11**

Electronic transitions in X-ray magnetic circular dichroism illustrated in a one-electron model. The transitions occur from a core shell (typically L shell) to empty conduction band states above the Fermi level, labeled $E_F$. The band occupation is shown here for an external magnetic field in the "down" direction. i.c. $\vec{H} \parallel -z$. Also shown is the correlation of the helicity and wavevector $\vec{k}$ for right and left circular polarization and the photon spin directions. If the light is incident in the $+z$ direction. The photon spin for right circularly polarized light is "up" and has the value $+\hbar$. The dichroism intensity is defined as the difference between a spectrum obtained with antiparallel relative orientation of photon spin and external field direction and a spectrum with parallel relative orientation. Adapt from Ref. 38.

# CHAPTER 3 EXPERIMENTAL RESULTS, ANALYSIS AND DISCUSSIONS

## 3.1. Systematical investigation of QW effect for continues Fe thickness

In this section, the author describes the experiment details for QW effect research, discusses and analyzes the characteristic QW effect systematically.

### 3.1.1. Experiment details for QW effect investigations

In this study, the author fabricated fully epitaxial Cr/ultrathin Fe/MgO/Fe junctions by molecular-beam epitaxy (MBE) and investigated the influence of post-annealing treatment for the ultrathin Fe layer on the QW effects.

Fully epitaxial MTJs consisting of Cr(001) (40 nm)/wedge shaped ultrathin Fe(001) ($t_{Fe}$ = 2–12 ML)/MgO(001) barrier/top Fe(001) (4 nm) were grown on MgO(001) substrates with a base pressure of $6\times10^{-8}$ Pa (see Fig. 3.1). The ultrathin Fe layer was prepared by post-annealing at ~250 ° C (sample B). For the MgO and top Fe layers, both samples were annealed at ~250 °C. The MgO thickness is 2.0 nm.

For the discussion of QW effects, first-derivative conductance curves (*dI/dV*) were measured using the conventional lock-in modulation technique *dI/dV* curves under a magnetic field of H = 1.6 kOe at room temperature. The voltage sign is defined with respect to the top electrode, which means that for positive (negative) voltage, electrons tunnel from (to) QW states below (above) the Fermi level.

The modulation voltage was 1 mV and the frequency was 1.30 kHz. The measurement details can be seen in Chapter 2.3 of this thesis. Because the wedge-shaped ultrathin Fe layer was grown on the same wafer, we could know the correct thickness in which large QW oscillations are observable.

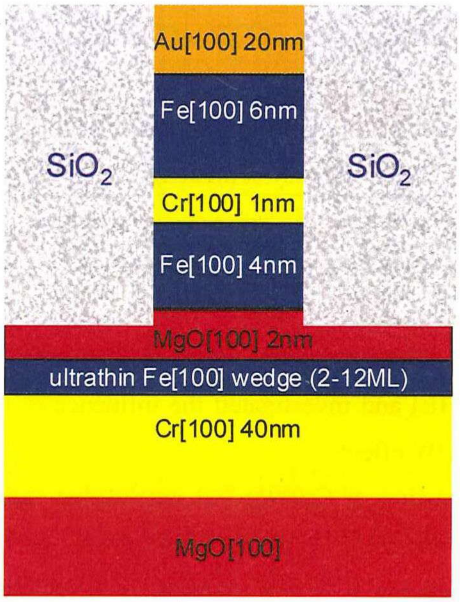

**Fig. 3.1**

Sample structure of Cr(001)/ wedge shaped ultrathin-Fe(001) (2-12ML)/ MgO(001)/ Fe(001) magnetic tunneling junction.

### 3.1.2. Fe thickness calibration and influence on *dI/dV* spectra

In order to get an accurate knowledge of the Fe thickness, the Fe deposition rate was calibrated by RHEED intensity oscillations on additional samples with uniform Fe thickness. This calibration work is important for our research, since the sensitivity Fe thickness influence on *dI/dV* curve.

An example, for a nominal Fe thickness of 9.05 ML, is given in Fig. 2. The oscillations show a period of 1 ML, which does not change with time. In addition, the oscillations are gradually damped and almost disappear after 8–9 ML. This damping oscillation amplitude originates from derivation from layer by layer growth. Therefore, a given nominal thickness corresponds to an average of some distribution of integer thicknesses. Improvement of the RHEED pattern upon annealing reflects the flattening of the surface and reduction of thickness distribution.

The inset of Fig. 3.2 shows the *dI/dV* curve of the corresponding MTJ (with 9.05 ML-thick Fe). A clear QW-related peak is observed around zero voltage in the dI/dV curve. We measured such *dI/dV* spectra for every MTJ of our sample with the Fe wedge. Fig. 3.3 (a) shows five curves for non-integer Fe thicknesses ranging between 8 ML and 9 ML. It can be seen that conductance oscillations are strongly sensitive to the thickness. In general, with increasing thickness, a peak vanishes (e.g. at +0.2 V in Fig. 3) while another grows (at -0.1 V). However, a shift to lower voltages is also observed, it is particularly obvious at large negative voltages. The peak positions are defined as the voltages at which the spectra show their local maxima.

Fig. 3.3 (b) shows the *dI/dV* curve of sample with 20nm thick bottom Fe, the curve shows the normal parabola shape without strong oscillation. Such result can be attributed to the absence of QW state since the large thickness of Fe.

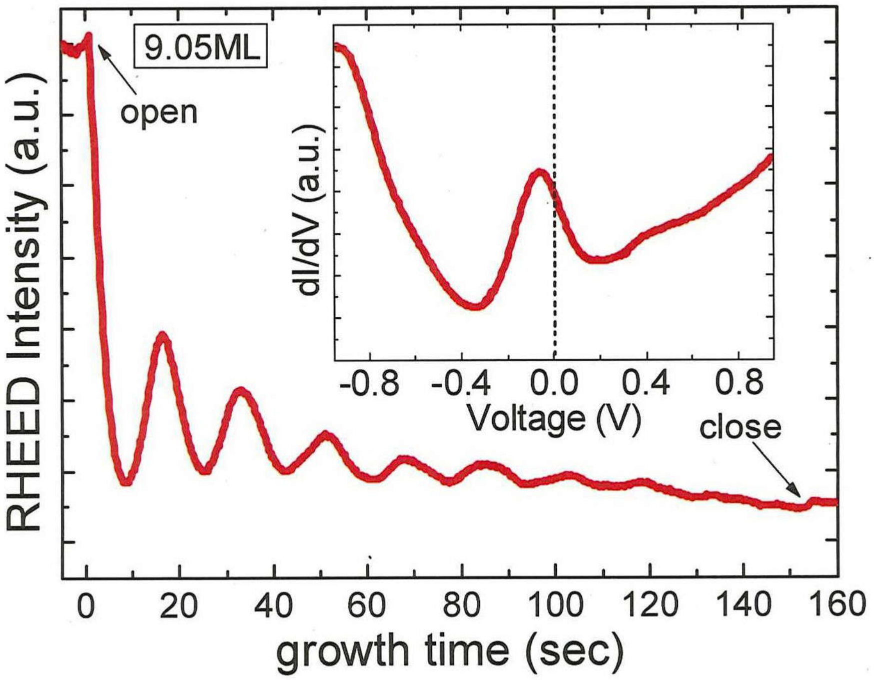

**Figure.3.2**

RHEED intensity oscillations during Fe growth on Cr(001). Inset: *dI/dV* curve of the corresponding MTJ.

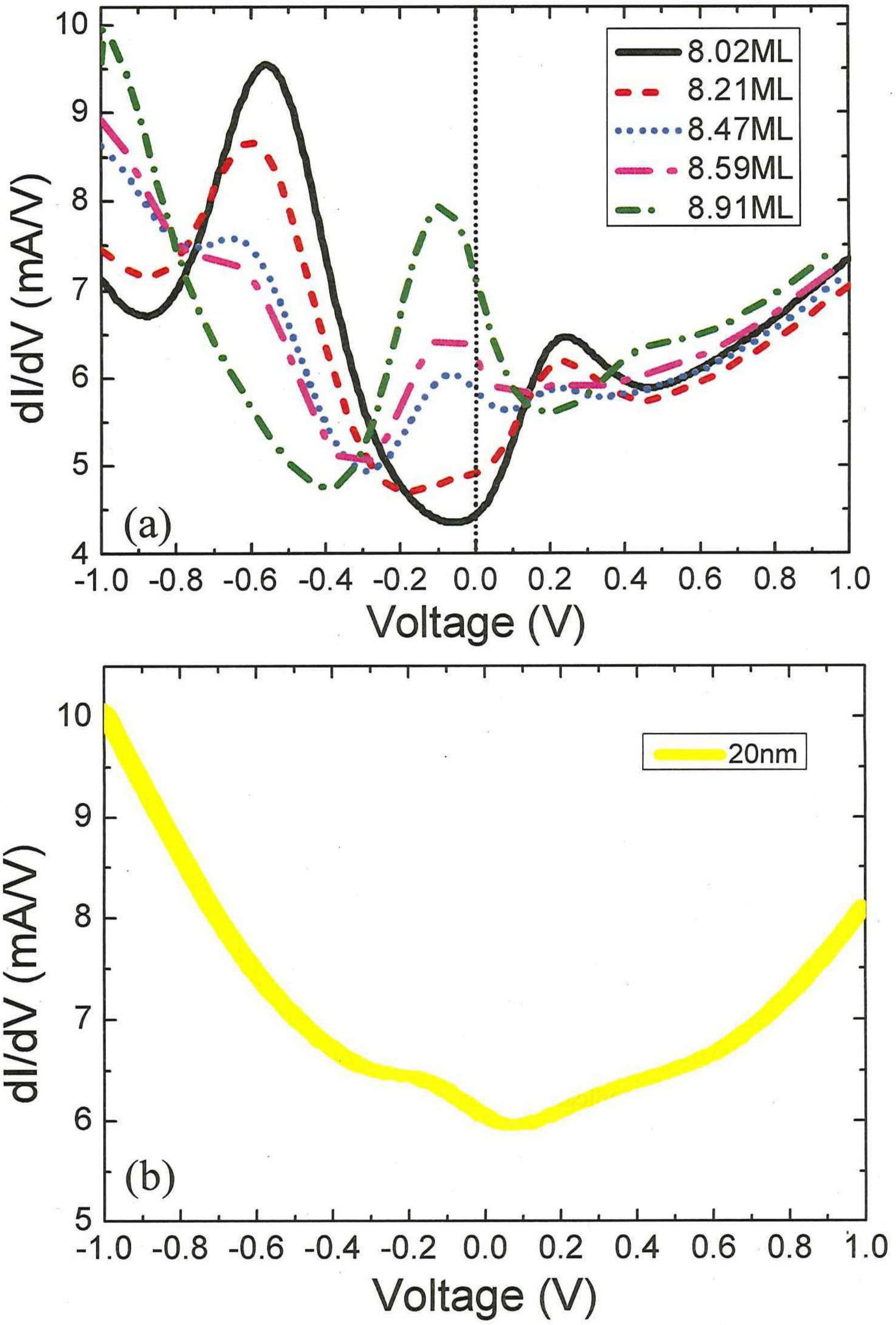

**Figure.3.3**

*dI/dV* curves of (a) five MTJs with various Fe thicknesses (QW); (b) MTJ with 20nm Fe (No QW).

### 3.1.3. Ultrathin Fe(001) layer thickness versus the QW resonant peak positions

A detailed investigation of QW states in MTJs with a wedge-shaped Fe layer is discussed here. The QW states are continuously mapped as a function of applied voltage and nominal Fe thickness, since *dI/dV* spectra for every MTJ of our sample with the Fe wedge were measured.

Fig. 3.4 shows all the *dI/dV* spectra measured along the wedge, providing a map of the QW states as a function of voltage and Fe thickness. The pattern is clearly spotted, with conductance maxima occurring exactly at integer thicknesses. Some intensity is seen between certain pairs of spots, resulting in the apparent continuous shift of the peaks to lower voltages while increasing the thickness.

As shown in Ref. 22 (see Fig. 1.10), in the case of a Cu QW observed by photoemission. The displacement of intensity maxima when varying the thickness was very similar to the present report. However, a major difference with our results is that, in Ref. 38 no maxima were observed at integer thicknesses. We propose two possible reasons for this difference: first, due to annealing, the actual distribution of thicknesses may be narrower in our films, which should yield conductance maxima at integer thicknesses; and second, we cannot deny the possibilities due to band structure details and discussed in Ref. [22, 39, 40]. We will discuss this point in the later section.

Based on the study of QWs, we also can discuss the electron mean free path in Fe at Fermi level for the electrons with majority spin $\Delta_1$ symmetry.

Theoretical calculation gives the expression of MTJ conductance (G) at parallel configuration as:

$$G=G_0+A\cos[2k_z d+\phi_0]e^{-3\kappa d} \qquad (1)$$

For the Fe/MgO/Fe(001) MTJs case, here $k_z$ means electron wave vector along Γ-H direction. $d$ denotes the bottom Fe thickness (ML), $\kappa^{-1}$ denotes electron mean free path in Fe with majority spin $\Delta_1$ symmetry. Equation (1) indicates that electron scattering damps oscillation exponentially with damping factor $3\kappa$.

The fitting curve in the right panel of Fig. 3.4 can be expressed as:

$$G=0.00593+0.00301\cos[2*0.47690\pi d+1.48871\pi]e^{-d/9.92199} \qquad (2)$$

Compare formula (1) and (2), we can easily deduce that:

$$G_0=0.00593(\mathrm{S}),\ A=0.00301(\mathrm{S}),\ k_z=0.47690\pi(\mathrm{ML}^{-1}),\ \phi_0=1.48871\pi,$$
$$\kappa^{-1}=3\times 9.92199(\mathrm{ML}),\ \text{so}\ \kappa^{-1}\approx 30\mathrm{ML}\ \text{or}\ 4.3\mathrm{nm}.$$

That means at Fermi level the mean free path of electrons with majority $\Delta_1$ state in Fe is around 4nm. This length is significantly longer than the other literatures reported before as around 1nm [17,41]. The longer mean free path reveals better crystal structure with less crystal defect in our sample. Since the $\kappa^{-1}$ can be influenced by crystal defect or film flatness, we are not sure our result reflects the real electron mean free path in Fe at Fermi level for the electrons with majority spin $\Delta_1$ symmetry. It may even longer if Fe film with better crystal structure and enhanced flatness is obtained.

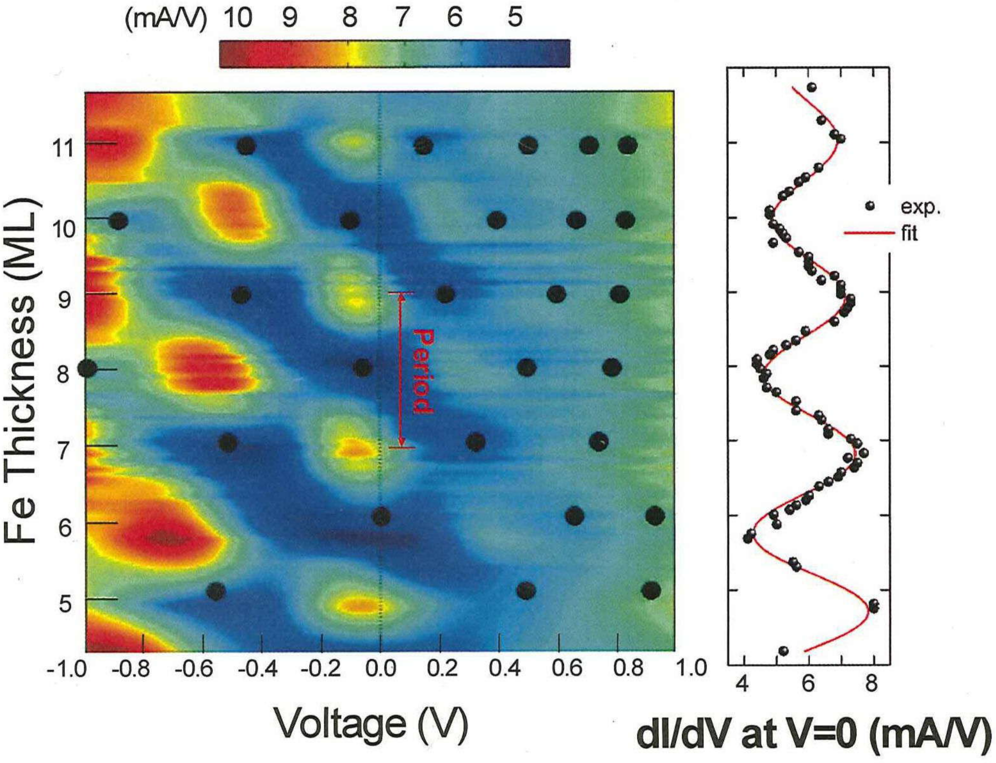

**Fig.3.4**

Left panel: Measured dI/dV values of Cr/Fe(*d*)/MgO/Fe MTJs as a function of Fe thickness d and applied voltage. Black dots: First-principles calculation from Ref. 20 for the Cr/Fe(*d*)/FeO(1)/MgO/Fe structure, where n and 1 are thicknesses in ML.

Right panel: Ultrathin Fe thickness dependence of conductance at 0 V, with the same vertical axis as that in left panel, indicating Fe thickness. Black dots: our experiment data. Red curve: fitting data. The color bar denotes the *dI/dV* values.

### 3.1.4. Correlations between Fe-QW and the Fe $\Delta_1\uparrow$ band

From Fe-QW research, the Fe $\Delta_1\uparrow$ band structure can be obtained. The discussion and analysis is presented in this section.

At Fermi level, the conductance (at zero bias) exhibits clear oscillatory behavior, as shown in Fig.3.5. We can easily read off the quantum resonance period ($p$) from the length between the intensity maxima are observed at 0 volt, as indicated by double-head arrow in Fig.3.5. By averaging all the 3 periods data, we got $p$=2.1±0.2 ML (1ML=$a_{Fe}$=$a$/2=1.433 Å, which denotes the lattice constants of bcc Fe) at zero voltage.

The period of these resonates corresponds to half the wavelength of a quantum-well state, like for the interference fringes of an optical interferometer (see in Fig.3.6). By using the relation as follows: $p=\lambda/2$ (here $\lambda$ denotes the envelope wavelength, which indicates that Fe $\Delta_1\uparrow$ wave is modulated by Bloch functions, since the presence of a periodic Fe atomic potential). We can derivate the wave vector $k$ of the so-called envelope function. This envelope function modulates a rapidly oscillating Bloch wave function that is derived from band-edge states in the quantum well. Then it can be expressed as:

$$k_{env}=k_{BZ}-k_F=2\pi/\lambda=\pi/p=0.47\pm0.05\ k_{BZ}\ (k_{BZ}=2\pi/a\ \text{units})$$

This yields a Fermi wavevector $k_F$ = 0.53±0.05 $k_{BZ}$. Theoretically [10], a value of $k_F$ = 0.44 $k_{BZ}$ is expected, see Fig.3.7 (a). Our larger value may reflect weaker band dispersion due to the reduced dimensionality.

In addition, by using Fourier transform, the entire Fe $\Delta_1\uparrow$ bulk-band structure can be obtained from QW states at different voltages as shown in Fig.3.7 (b). A good agreement was obtained with the theatrical calculated band (see in Fig.3.7(a)).

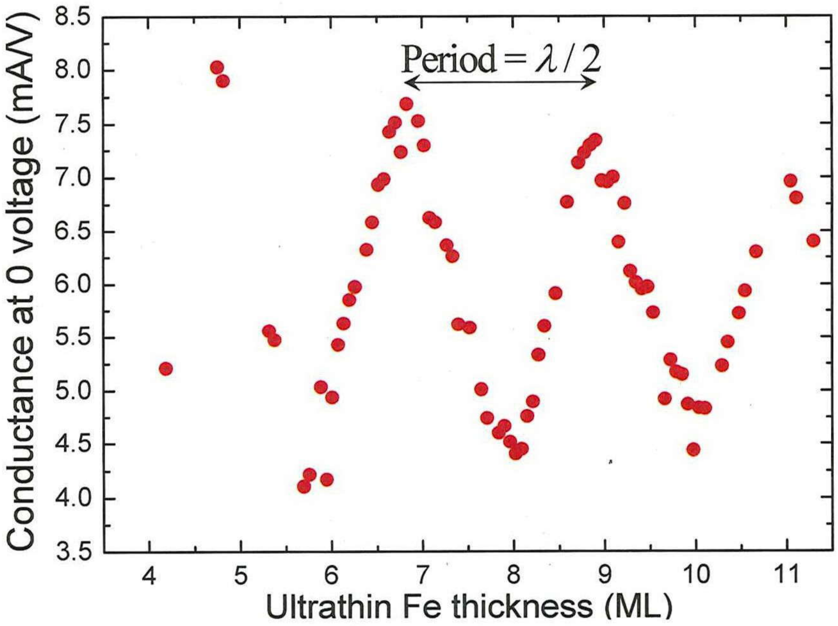

**Fig.3.5**

Ultrathin Fe thickness dependence of conductance at 0 V. Oscillations of the conductance intensity with quantum-well thickness can be observed.

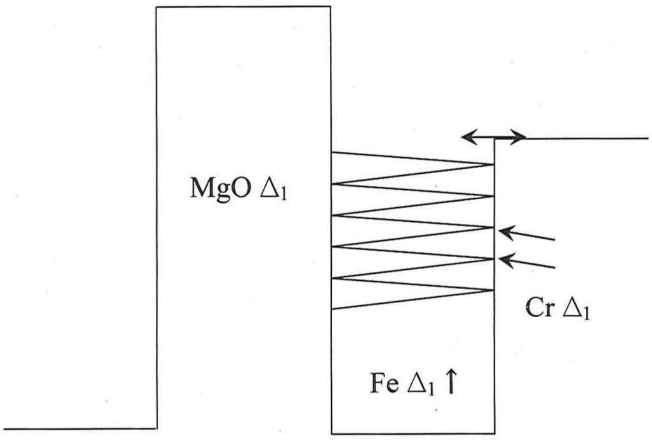

**Fig.3.6**

$\Delta_1$ Band diagram in Cr/ultrathin Fe/MgO QW structure.

The period of these oscillations corresponds to half the wavelength of a quantum-well state, like for the interference fringes of an optical interferometer. Oscillations of the conductance intensity with quantum-well thickness, measured at the two energies that are indicated by arrows.

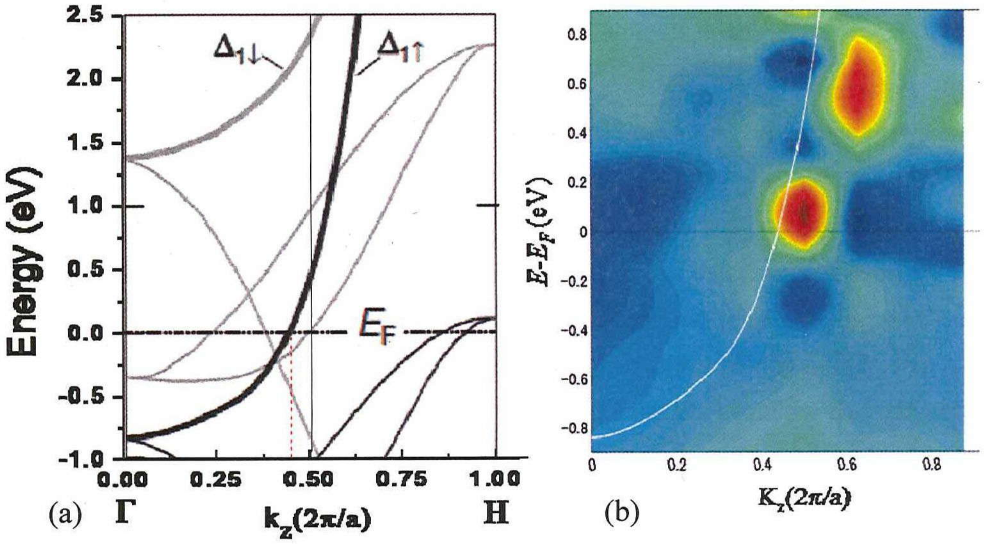

**Fig.3.7**

Band dispersion of bcc Fe in the (001) (Γ–H) direction.

(a) First principle calculation obtained. Adapt from Ref.10.

(b) Our experiment data obtained. White line denotes the theatrical Fe $\Delta_1$ band as show in the thick black line in (a).

## 3.2. Interfaces status investigations and influence on the QW effect

We now discuss the values of resonant energy positions. In this aspect, our results agree well with the experimental work done by T. Niizeki et al. [17]. In particular, conductance peaks are observed near zero bias for odd Fe thicknesses. An *ab* initio calculation, which assumed that 1 ML FeO was present at the Fe/MgO interface, predicted the resonant peaks positions [20], indicated by filled black circles in Fig. 3.4. There is systematically a 1 ML difference with our findings. The origin of such discrepancy will be discussed in this section.

Ideally, one should compare our results with the theory for the same Cr/Fe/MgO structure, but the calculations without FeO have not been made so far. A possible reason for this 1 ML difference could be the presence of an "invalidated" Fe layer at either the Fe/MgO interface (Fe oxidization) or at the Cr/Fe interface (intermixed layer). Indeed, $FeO_x$ or $FeCr_x$ layers could form additional potential barriers for $\Delta_1$ states, thereby reducing the QW thickness.

### 3.2.1. MOKE measurement in Cr/Fe (0-12.6 ML)/MgO (2 nm) sample

In order to study the interfaces in our samples, we measured the magneto-optical Kerr effect (MOKE) of a Cr/Fe (0-12.6 ML)/MgO (2 nm) sample (see Fig.3.8), which was grown in the same conditions as those used for our MTJs.

We measured 19 points from bottom to the top of sample. The measurement diagram can be seen in Fig.3.9.

All the MOKE measurement data can be see in Fig. 3.10. Obviously change can be observed since the increase of total magnetic moment in Fe films.

Fig. 3.11 shows a linear decrease of the MOKE signal when decreasing the Fe thickness. The error bar gives the range of possible error, which may due to the unstableness of deposition ratio, laser point size and so on.

The signal drops to zero at a finite thickness of 1.7±0.2 ML, which strongly suggests the presence of a nonmagnetic layer at the interface. This layer could be either an Fe-Cr alloy or an Fe oxide.

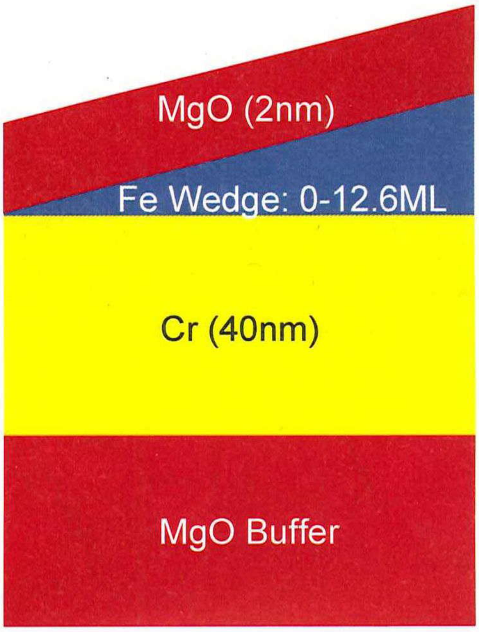

**Fig.3.8**

Sample structure for MOKE measurement

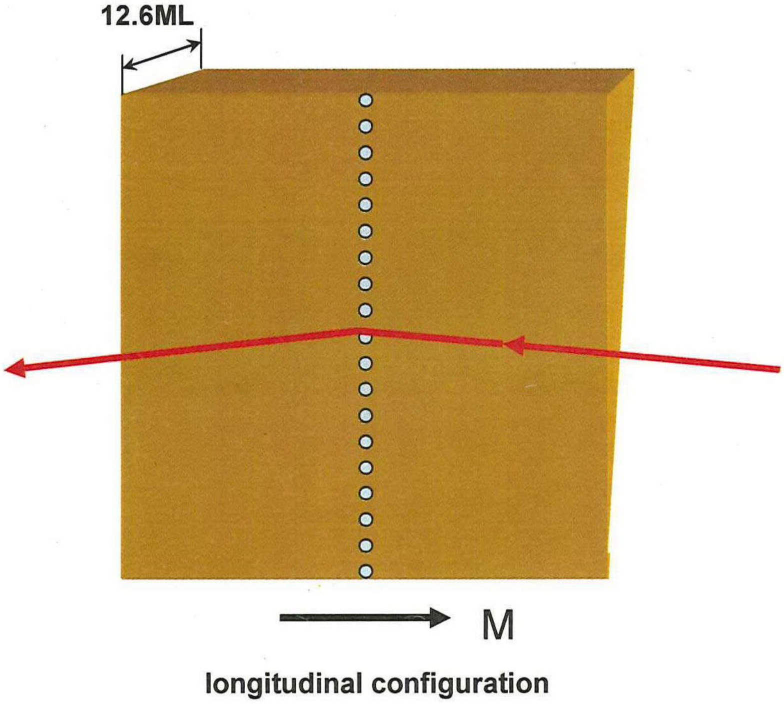

**Fig.3.9**

MOKE measurement at longitudinal configuration. The arrows indicate the laser and magnetic filed direction respectively; spots indicate the measurement positions.

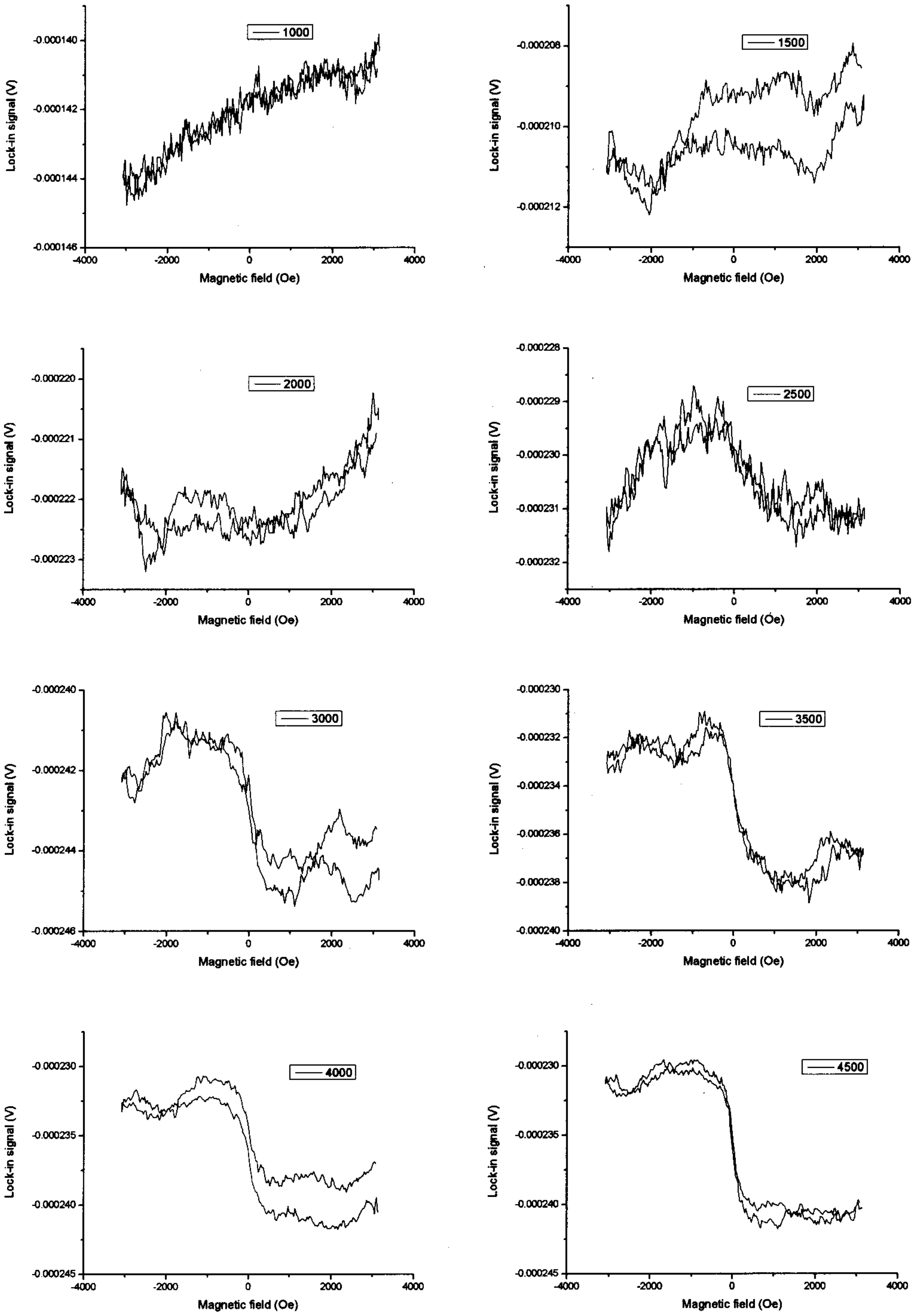
1000
Lock-in signal (V)
-0.000140
-0.000142
-0.000144
-0.000146
Magnetic field (Oe)
-4000
-2000
0
2000
4000
1500
-0.000208
-0.000210
-0.000212
2000
-0.000220
-0.000221
-0.000222
-0.000223
2500
-0.000228
-0.000229
-0.000230
-0.000231
-0.000232
3000
-0.000240
-0.000242
-0.000244
-0.000246
3500
-0.000230
-0.000232
-0.000234
-0.000236
-0.000238
-0.000240
4000
-0.000230
-0.000235
-0.000240
-0.000245
4500

**Fig. 3.10**

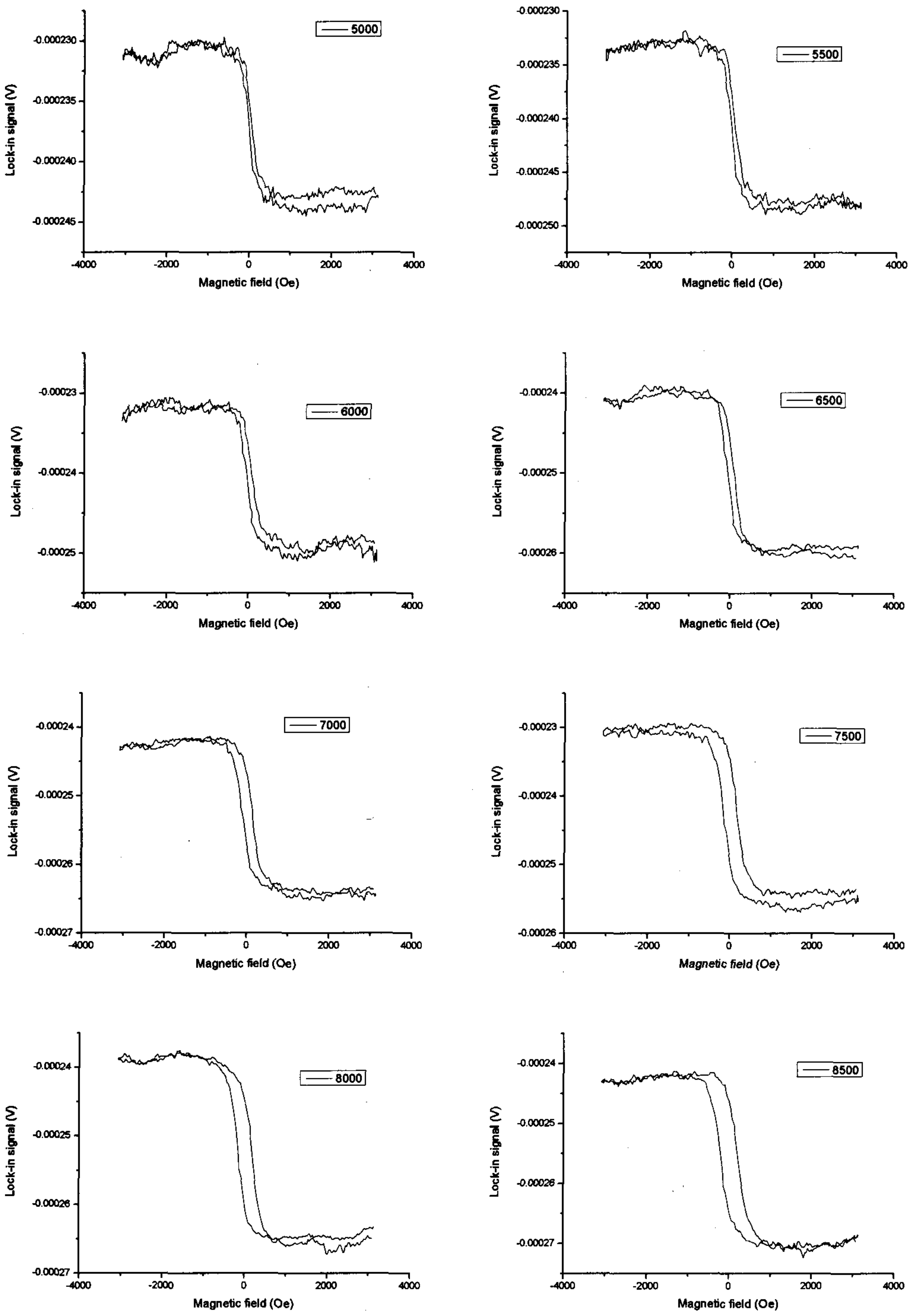
5000
Lock-in signal (V)
-0.000230
-0.000235
-0.000240
-0.000245
Magnetic field (Oe)
-4000
-2000
0
2000
4000
5500
Lock-in signal (V)
-0.000230
-0.000235
-0.000240
-0.000245
-0.000250
Magnetic field (Oe)
-4000
-2000
0
2000
4000
6000
Lock-in signal (V)
-0.00023
-0.00024
-0.00025
Magnetic field (Oe)
-4000
-2000
0
2000
4000
6500
Lock-in signal (V)
-0.00024
-0.00025
-0.00026
Magnetic field (Oe)
-4000
-2000
0
2000
4000
7000
Lock-in signal (V)
-0.00024
-0.00025
-0.00026
-0.00027
Magnetic field (Oe)
-4000
-2000
0
2000
4000
7500
Lock-in signal (V)
-0.00023
-0.00024
-0.00025
-0.00026
Magnetic field (Oe)
-4000
-2000
0
2000
4000
8000
Lock-in signal (V)
-0.00024
-0.00025
-0.00026
-0.00027
Magnetic field (Oe)
-4000
-2000
0
2000
4000
8500
Lock-in signal (V)
-0.00024
-0.00025
-0.00026
-0.00027
Magnetic field (Oe)
-4000
-2000
0
2000
4000

**Fig. 3.10**

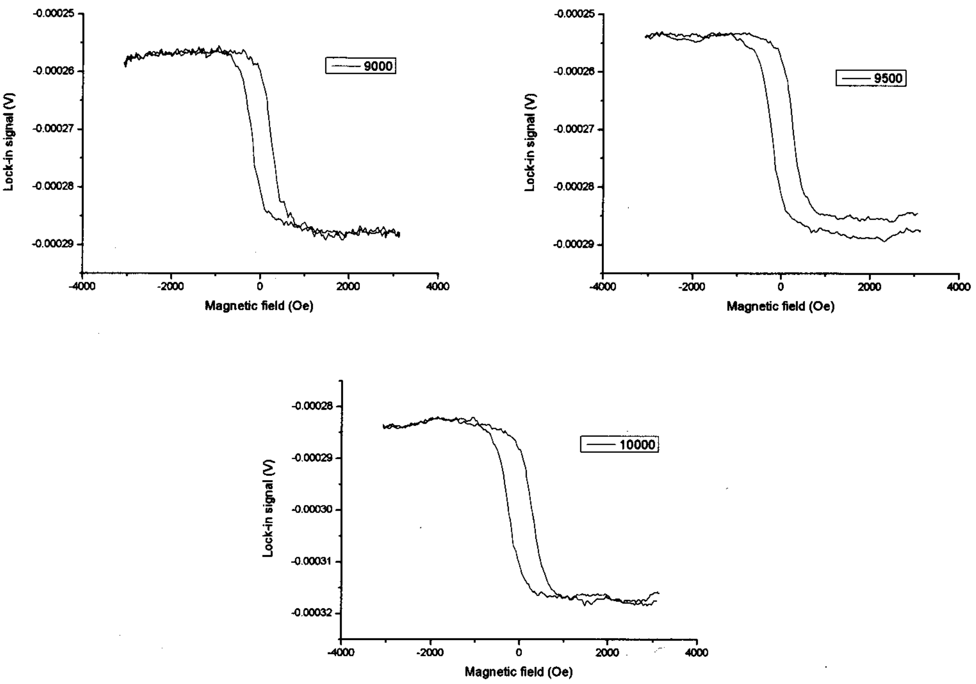

**Fig. 3.10**

MOKE measurement for all the positions. Obviously change can be observed since the increase of total magnetic moment in Fe films. The increase numbers indicate the increase of Fe thickness corresponding to the 19 measured positions.

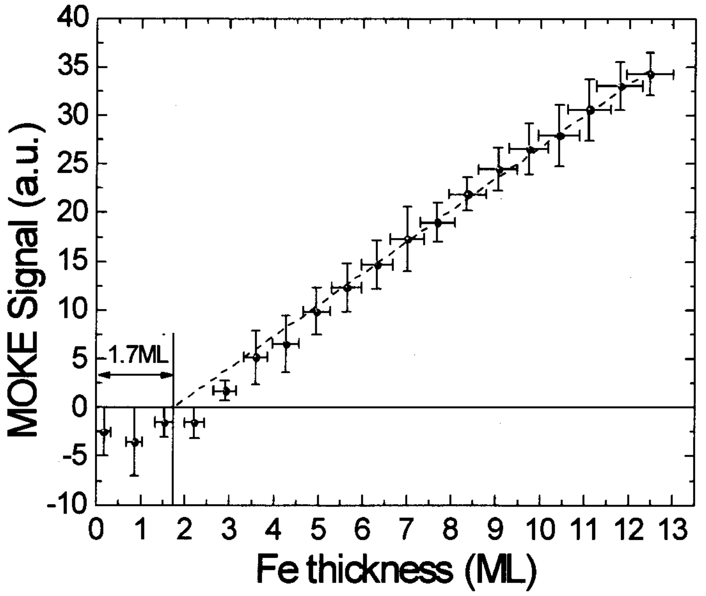

**Fig. 3.11**

Fe thickness dependence of the MOKE signal. The dashed line is a linear fit of data for thicknesses above 6 ML.

### 3.2.2. Interface status investigation by XAS and MCD measurement

To gain further knowledge on the interfaces, XAS and XMCD measurements were conducted on Cr/Fe(1.5 ML)/MgO(1 nm) (sample A) and an MgO/Fe(30 nm)/MgO(1 nm) reference sample for bulk Fe (sample B). These samples were grown in the same conditions as those in which the MTJs were grown, with the exception that the 1.5 ML-thick Fe film was not annealed.

The bottom panel in Fig. 3.12 shows our measured Fe $L_{2,3}$ edge spectra. The pre-edge XAS values were set to zero and the curves were normalized to the same $L_3$ intensity. Due to the extended X-ray fine structure (EXAFS) of Cr, the baseline of sample A exhibits strong oscillations which prevent the application of sum rules. We therefore restrict our discussion to a qualitative analysis. The upper panel in Fig. 3.12 shows reference spectra of metal Fe and Fe oxides from Ref. 42. As can be seen, the XAS lineshape is very sensitive to Fe oxidation. Spectra of samples A and B have a very similar lineshape and no multiplet is observed. Therefore, we can directly exclude the presence of $Fe_2O_3$ and $Fe_3O_4$ oxides. The main difference between both spectra is the MCD reduction by roughly 40% in sample A, which means a similar reduction in the magnetic moment. There could be several explanations for this: (i) The presence of antiferromagnetic FeO at the Fe/MgO interface. However, the characteristic $L_3$ pre-peak and $L_2$ structure of FeO (upper panel in Fig. 3.12) are not observed in our spectra. Therefore, given the very small amount of Fe in our sample, we can rule out the presence of any Fe oxide at the Fe/MgO interface. This result agrees with previous studies [30, 33, 43]. (ii) A reduced Curie temperature in ultrathin Fe [44]. (iii) An intrinsic reduction of the magnetic moment at the interfaces. Such reduction is expected at the Fe/Cr interface [45, 46], whereas an increase has been predicted and measured at the Fe/MgO interface [30,47]. (iv) Intermixing with Cr, possibly place exchange at the interface. Fe-Cr intermixing at room temperature has actually been reported in Ref. 33 and is expected to reduce the Fe magnetic moment [48]. The presence of an interfacial Fe-Cr alloy could account for our transport, MOKE and MCD results. In MOKE measurements, the magnetic signal vanishes for Fe thicknesses below 1.7±0.2 ML. However, we observe a sizable MCD signal with 1.5 ML of Fe. This disagreement is possibly due to the annealing process for the sample measured by MOKE, which may increase the Fe-Cr intermixing. The effective thickness of Fe QWs could be reduced because of this interfacial Fe-Cr alloy.

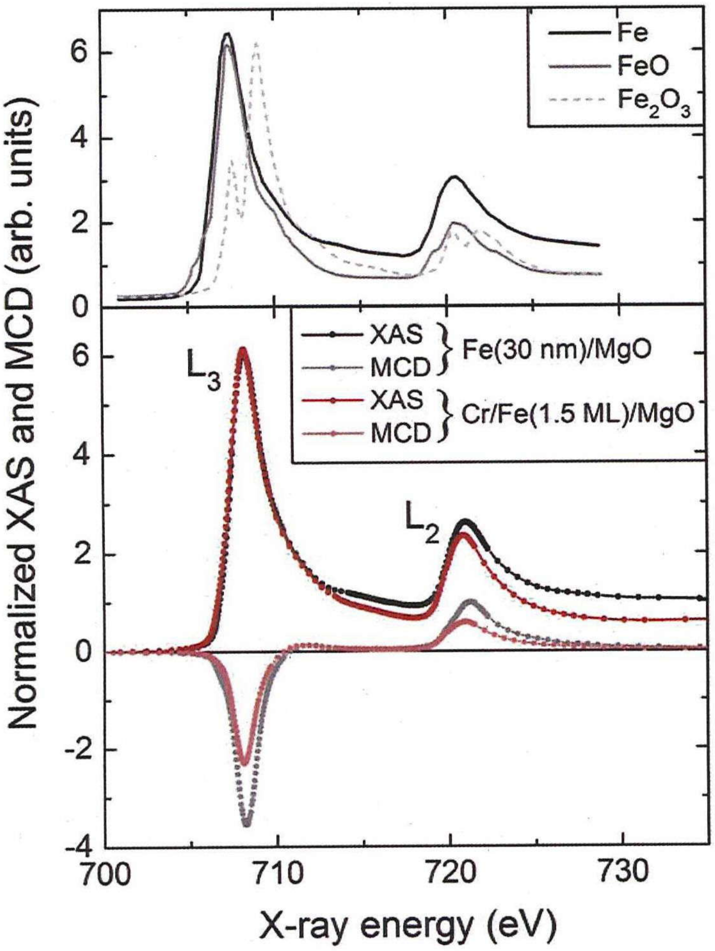

**Fig.3.12**

Upper panel: measured XAS spectra for Fe metal and oxides, from Ref. 42. Lower panel: measured XAS and MCD spectra of Fe (30nm)/MgO and Cr/Fe (1.5ML)/MgO.

### 3.2.3. Fe-QW state features analysis

We would like to give an explanation for the features of QW state in crystalline Fe.

As we know the phase accumulation model (PAM) has worked very successfully in the elucidation of QW state energies in metallic thin films based on photoemission measurement results, such as thin Ag on Fe(001)[39,49], Cu on fcc Co(001) [22,40,49] and so on. Here the author applied the same method to analyze Fe-QW state, and compare the results with previously researched Cu-QW or Ag-QW states.

One can calculate the position of the QW state by using PAM in which the quantization condition is written as:

$$2k(E)d_{Fe}+\phi_{MgO}+\phi_{Cr}=2\pi n, \quad (n=\text{integer}) \qquad (3)$$

Where $\phi_{MgO}$ and $\phi_{Cr}$ are the phase gains of the electron wave function upon reflection at the Fe/MgO and Fe/Cr interfaces, respectively. The $d_{Fe}$ is the thickness of the Fe layer, $n$ is the number of half wavelengths confined inside the quantum well, and $k(E)$ describes the Fe $\Delta_1\uparrow$ band along the Fe(001) direction.

In those studies, one of the important features should be addressed is that Bloch functions influence on the propagating electrons in the initial QW state, because of the presence of a periodic atomic potential in the overlayer film result in the possibility of Bragg scattering. An *significant* result is that, based on the PAM, the electron wavefunctions were no longer described just as a sum of two waves, propagating in opposite directions (with wavevectors $k$ and $-k$) since reflections at the film boundaries, but instead by four waves, the two already considered and two additional components which result from the Bragg reflections of each of these. See Fig. 3.13 (a).

These two additional waves have wavevectors $(k-g)$ and $-(k-g)$, where $g$ is a reciprocal lattice vector. Commonly, QW states occur with $k$ values which are reasonably close to a Brillouin zone boundary. This is because such states must occur in a substrate band gap (and hence must have real components of k in the substrate which are at such a boundary), and if the overlayer film layer spacing is similar to that of the substrate this will often mean one is also reasonably close to a band edge in the film. For different structural phases, of course, this need not be the case. If it is so, however, then the QW wavevector $k$ and its Bragg-scattered wavevector $(k-g)$ will be closely similar, similar to the effect of beats in classical waves, and combining them will produce a modulating envelope with a spatial period much longer than that of the original electron wave. The consequence of combining all four waves is thus to produce a spatially modulated standing wave. This modulation is commonly referred to as the envelope function [51].

Notice, however, Fe thickness as integer multiples ($N$) of the atomic spacing, so $d = Na$ and the reciprocal lattice vector perpendicular to the surface associated with the first Brillouin zone is $g = 2k_{BZ} = 2\pi/a$ so $2k_{BZ}d_{Fe} = 2N\pi$, which means that one can rewrite equation (3) as

$$2(k-k_{BZ})d_{Fe}+\phi_{MgO}+\phi_{Cr}=2\pi(n-N)$$
$$\text{or } 2(k_{BZ}-k)d_{Fe}-\phi_{MgO}-\phi_{Cr}=2\pi\upsilon \qquad (4)$$

Now $(k_{BZ}-k)$ is the wavevector of the envelope function $k_{env}$, so equation (4) appears to show that it is the matching of the envelope function phase which is the fundamental requirement.

We have just simply added the same amount of phase to both sides of equation (3), and the result is really more an issue of 'text book' than of fundamental physics. Equation (4) would be no less true if there were no significant periodic atomic potential in the film and thus no significant Bragg scattering (and hence no envelope function). Furthermore, the energy of the QW state is determined by $k$, and this value is found from matching the associated electron wavelength to the well as defined by equation (3), with no reference to the Brillouin zone wavevector. What equation (4) shows, however, is that, having achieved this matching in $k$, one also has a similar matching of the envelope arising from the Bragg scattering within the periodic potential of the film. See Fig.3.13 (b).

In addition, near the zone boundary the wave function displays an amplitude modulation having a long period envelope with wave vector $k_{env}$. Near the zone center, on the other hand, we have QW functions but with a small short- wavelength ripple. This can see in Fig. 3.14 and Ref. 39.

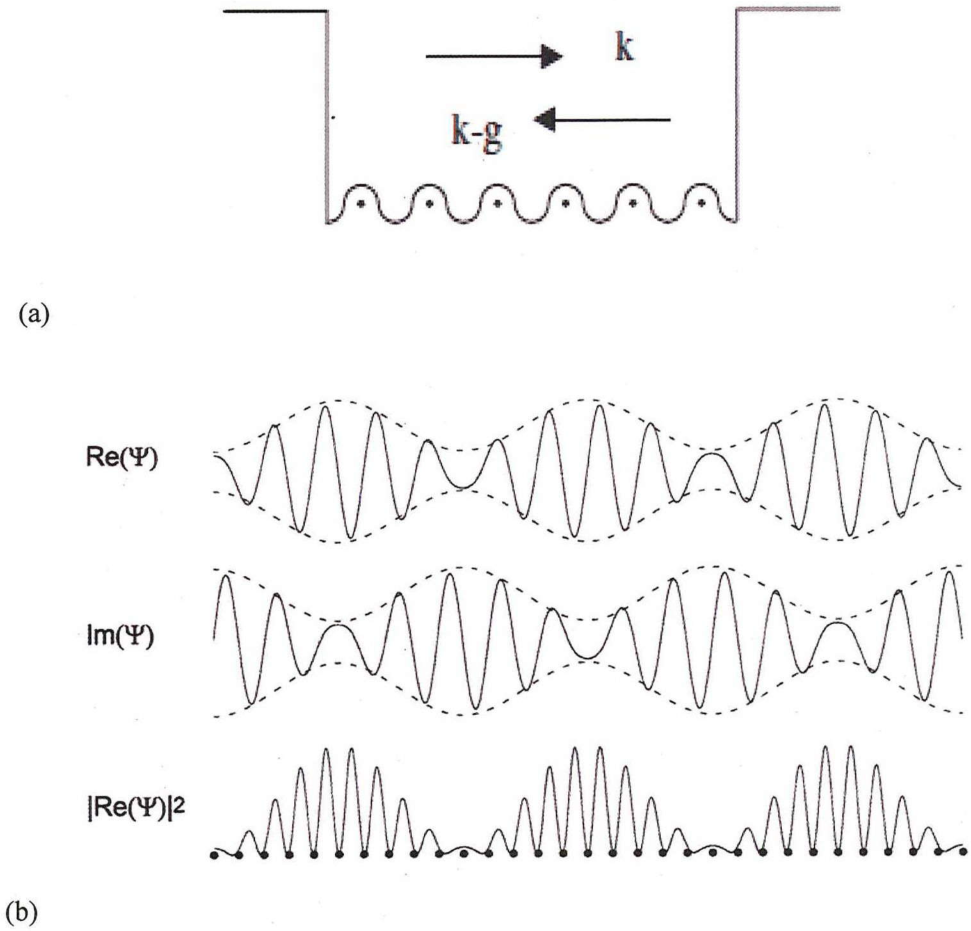

**Fig.3.13**

(a) A corrugated box in which the plane wave *k* is back-diffracted into plane wave *k–g*.

(b) Wavefunctions in a corrugated box. On moving away from the Brillouin zone boundary, the QW wavefunction becomes modulated by an envelope function (dashed curves) characterized by a wavevector $2k_{\mathrm{env}}$ where $k_{\mathrm{env}} = k_{\mathrm{BZ}} - k$. Adapt from Ref.[50].

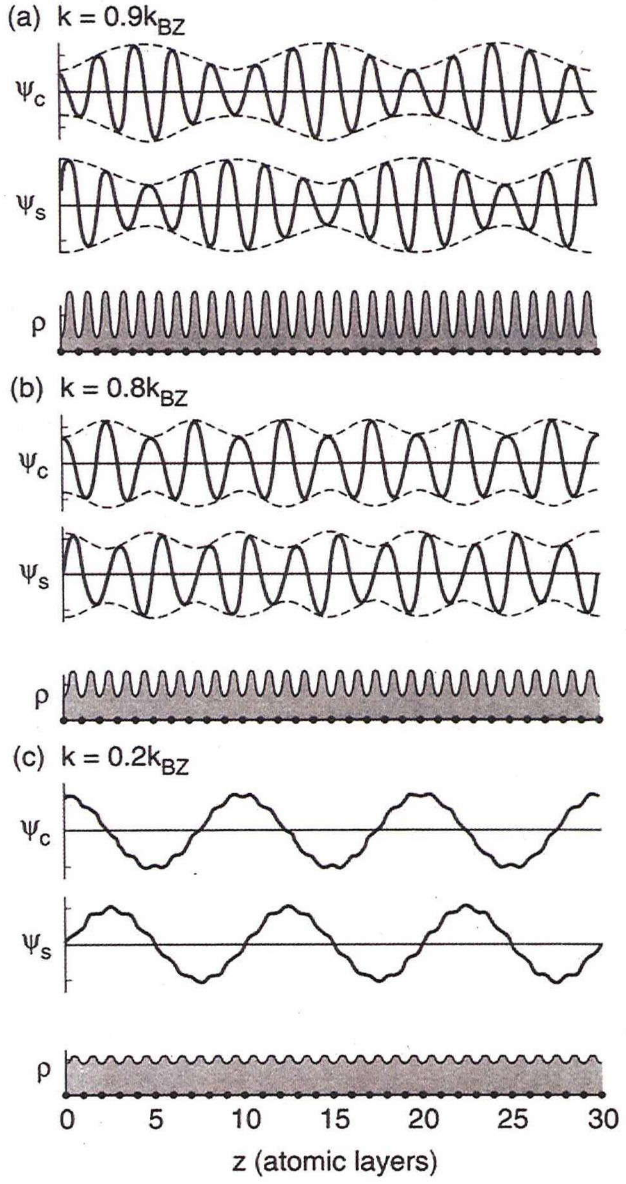

**Fig.3.14**

Wave functions generated by the two-band NFE model for Ag(001) for various values of wave vector *k*: (a) $k$ =0.9$k_{\mathrm{BZ}}$ ; (b) k =0.9$k_{\mathrm{BZ}}$; and (c) k =0.2$k_{\mathrm{BZ}}$. $\psi_c$, and$\psi_s$, are the cosinelike and sinelike QW functions, respectively, and $\rho$ is the charge density $|\psi_c \pm \psi_s|^2$ of the associated Bloch functions. The dashed curves in (a) and (b) indicate the envelope function. Adapt from Ref. 39.

## 3.3 Modulation of TMR by control QW states

The author describes experiment results of tailing of interface flatness be an efficient way to tune QW effect. In addition, TMR ratio influenced by QW state is also been illustrated.

### 3.3.1. Interface flatness influence on QW effect

Epitaxial growth of each layer was confirmed by examining the reflection high-energy electron diffraction (RHEED) patterns. In Fig. 3.15(a) and (b), RHEED patterns taken for the Fe ultrathin layer surface without annealing and with annealing at ~250 °C are shown, respectively. In Fig. 3.15(c) and (d), those for the MgO barrier surfaces are shown. In Fig. 3.15(b), we can see a sharp streak pattern from the annealed ultrathin Fe layer, indicating an atomically flat surface. On the other hand, the pattern of the Fe layer without annealing is a little spotty (Fig. 3.15(a)) because of its roughness. Such difference can be seen also for the MgO layer (Fig. 3.15(c) and (d)).

Fig. 3.16 shows the Fe thickness dependence of the *dI/dV* curves for (a) sample A, $t_{Fe} = 6, 8, 10$ ML, (b) sample A, $t_{Fe} = 7, 9, 11$ ML, (c) sample B, $t_{Fe} = 6, 8, 10$ ML, and (d) sample B, $t_{Fe} = 7, 9, 11$ ML obtained under an in-plane external magnetic field of 1.6 kOe. The magnetization in the ultrathin Fe free layer and that of the Fe reference layer are in an almost parallel configuration for all cases. It should be noted that the parallel configuration is well defined although the antiparallel configuration is not stable, as seen in the Fig. 3.17. A positive bias voltage is defined as the voltage in which the current flow from the top Fe layer to the bottom ultrathin Fe layer. The dynamic conductance (*dI/dV*) spectra essentially show a parabolic curve added to a constant conductance. The parabolic increase in dynamic conductance in the high bias region is a consequence of nonlinear conductance in the tunneling junctions [37]. In addition to the parabolic curve, clear oscillatory components were observed at room temperature in all samples, especially in the negative bias directions. In general, unoccupied states rather than occupied states contribute to the dynamics conductance. Therefore, in this measurement, since the tunneling electrons flow from the top Fe layer to the bottom Fe ultrathin layer under negative bias, the electronic structure of the ultrathin Fe(001) layer can be effectively observed in the negative bias region. From this discussion, the observed oscillation should come from the QW states formed in the ultrathin Fe layer. Though the two samples are different in terms of their junction size and MgO barrier thickness, the differences should not influence the discussion about the comparison of the peak amplitude: since the oscillation in conductance induced by the MgO layer thickness change (~2%) [7,52] is much smaller than the QWS oscillation (around 100%), the difference in the junction size should not affect the formation of

QW states in principle. Comparing the results from sample A and sample B, the conductance peak height is strongly enhanced for the post-annealed sample. To discuss this point quantitatively, we evaluated the modulation ratio of the tunneling conductance from the following equation.

$$\text{Oscillation Ratio (\%)} = \frac{\left.\frac{dI}{dV}\right|_{\text{peak}} - \left.\frac{dI}{dV}\right|_{\text{dip}}}{\left.\frac{dI}{dV}\right|_{\text{dip}}} \times 100$$

For the case of sample A with 9 ML ultrathin Fe, the oscillation ratio is only about 8% near zero voltage (the positions of the peak and the dip are indicated by arrows in the figures) while it is 72% for sample B with the same thickness of ultrathin Fe. The oscillation ratio becomes 150% for sample B with 6 ML ultrathin Fe. This value is higher than that in previous results [17], which showed about 90% amplitude at 6 K for the same thickness. This enhancement should be attributed to the improvement of the flatness of the ultrathin Fe layer by the appropriate annealing treatment.

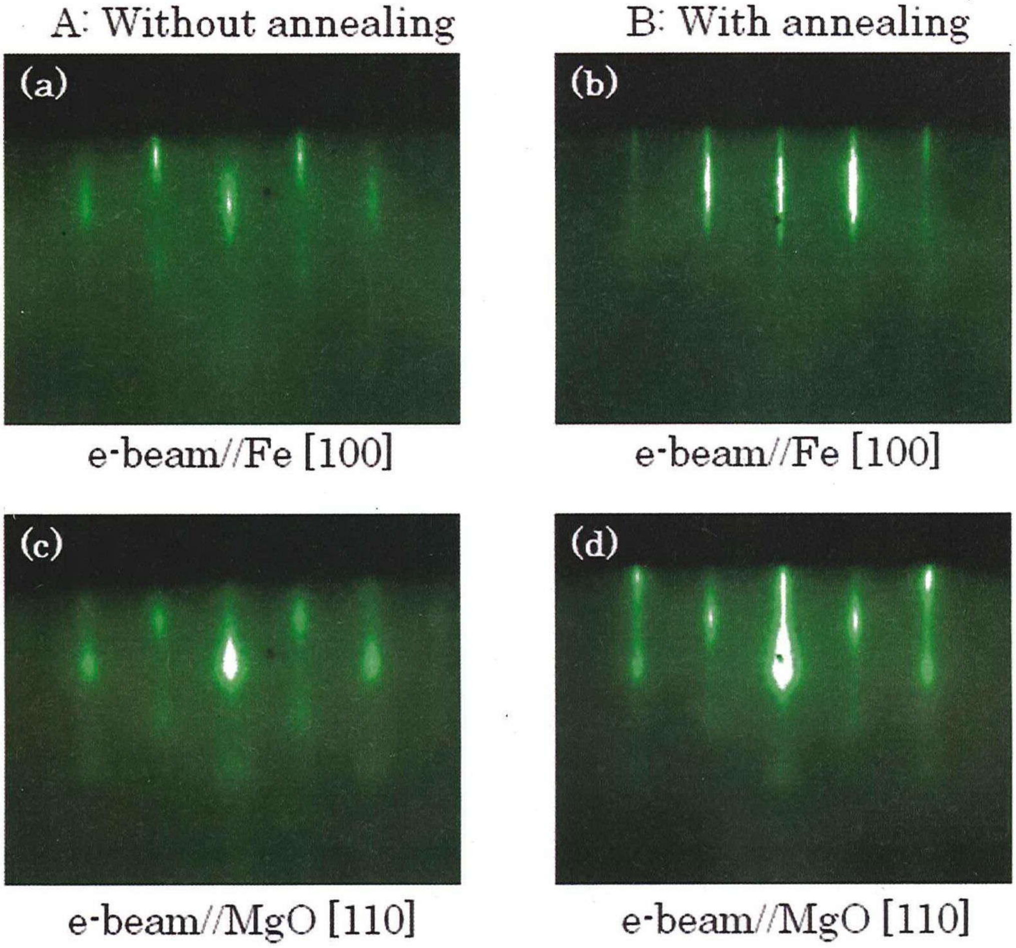

**Fig. 3.15**

RHEED pattern observed for the sample A (without annealing) and the sample B (with annealing). Upper ((a) and (b)) and lower ((c) and (d)) rows show RHEED patterns for the ultrathin Fe surface and the MgO barrier layer surface, respectively.

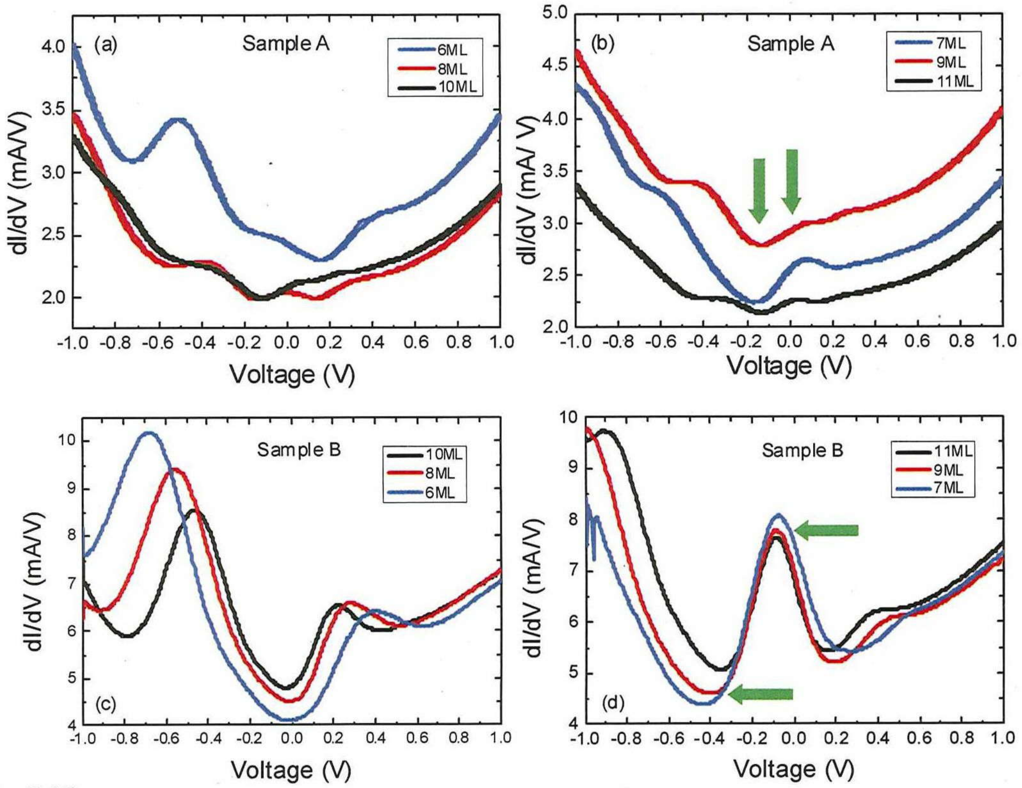

**Fig. 3.16**

The differential conductance spectra under the magnetic field of H=1.6 k Oe for sample A (a) $t_{Fe}$ = 6,8,10 ML and (b) $t_{Fe}$ = 7,9,11 ML and for sample B (c) $t_{Fe}$ = 6,8,10 ML and (d) $t_{Fe}$ = 7,9,11 ML. The ultrathin Fe layer was not annealed after the room temperature deposition for the sample A and post-annealed at 200 °C for the sample B.

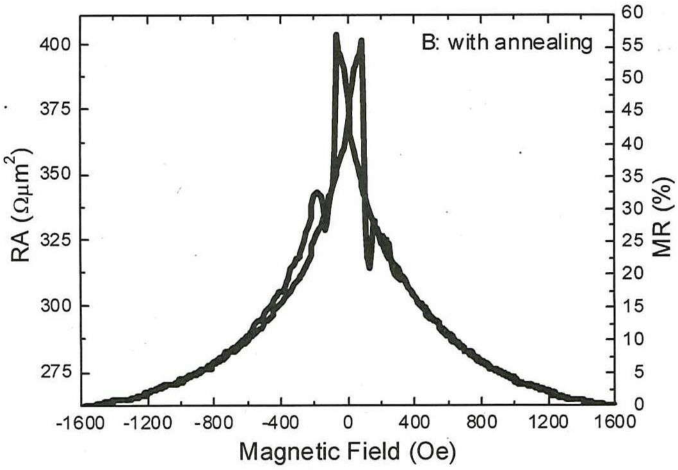

**Fig. 3.17**

RA and MR curve for the sample B with 10 ML thickness of ultrathin Fe. The MR ratio is about 55%.

### 3.3.2. TMR modulated by QW effect

Clear quantum oscillations of differential TMR in sample B was also observed, as shown in Fig. 3.5. Here the differential TMR was calculated from the following equation.

$$\text{Differential TMR (\%)} = \frac{\left.\frac{dI}{dV}\right|_{H=1.6\text{ kOe}} - \left.\frac{dI}{dV}\right|_{H=0\text{ Oe}}}{\left.\frac{dI}{dV}\right|_{H=0\text{ Oe}}} \times 100$$

The differential TMR effect is strongly modulated, and clear features of oscillating components are observed at the bias voltages which correspond to the resonant peaks observed in the *dI/dV* curves under the magnetic field H = 1.6 kOe (see Fig. 3.18). These are clear indications of the QW effects on the spin-dependent tunneling.

By controlling the thickness of the ultrathin Fe layer and the bias voltages, we can tune the TMR effect through the QW effects in this device. The negative differential MR in Fig. 3.18 may originate from the strong tuning of QW effects. Negative differential MR can also be observed for the sample with good antiparallel configuration.

We also investigated the Fe thickness dependence of TMR, basically the TMR increases with the Fe thickness with a little QW modulated oscillation. From Fig.3.19, we can see that, basically the TMR increases with the Fe thickness with a little oscillation modulated by QW state.

Such weak modulation should be attributed to the imperfect antiparallel configuration in our MTJs, since the complex domain in ultrathin Fe electrode.

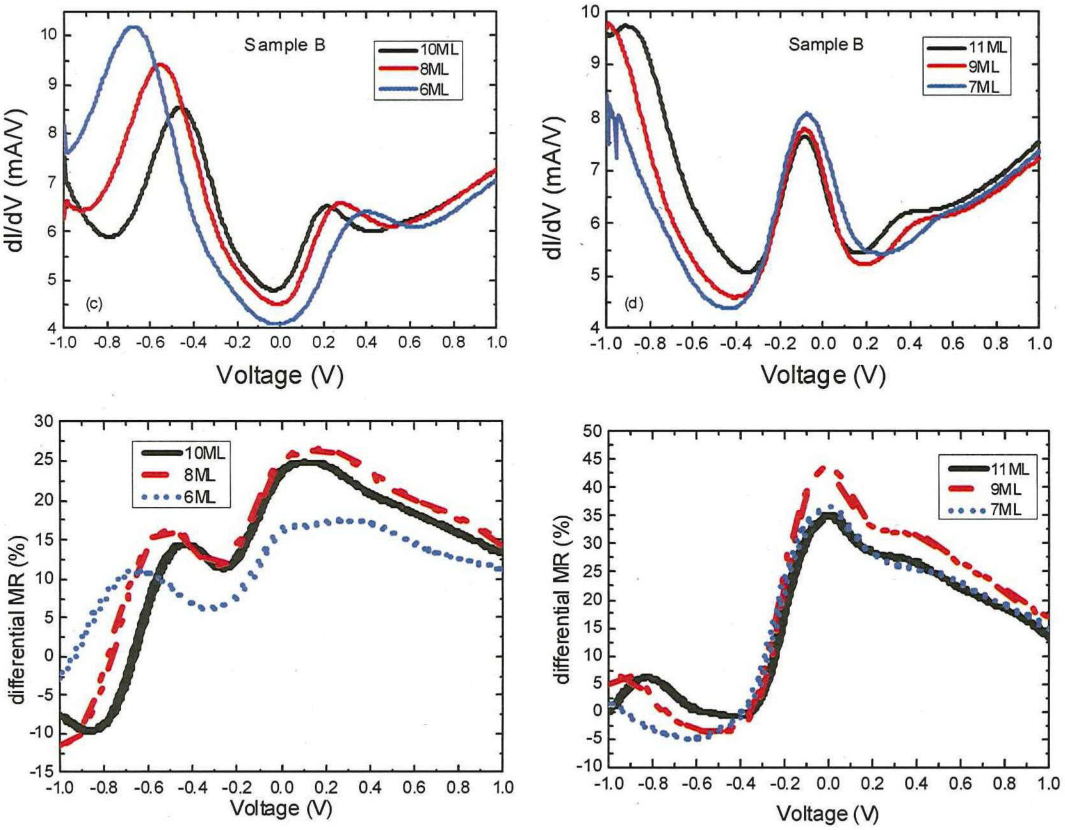

**Fig. 3.18**

Upper panels:

*dI/dV* cureve for sample B with $t_{Fe}$ =6, 8, 10 ML and $t_{Fe}$ = 7, 9, 11 ML.

Bottom panels:

Bias voltage dependence of differential TMR ratio for the sample B with $t_{Fe}$ =6, 8, 10 ML and $t_{Fe}$ = 7, 9, 11 ML, respectively. The negative differential MR can be originated from the strong tuning of QW effects. The negative differential MR also can be observed for the sample with good antiparallel configuration.

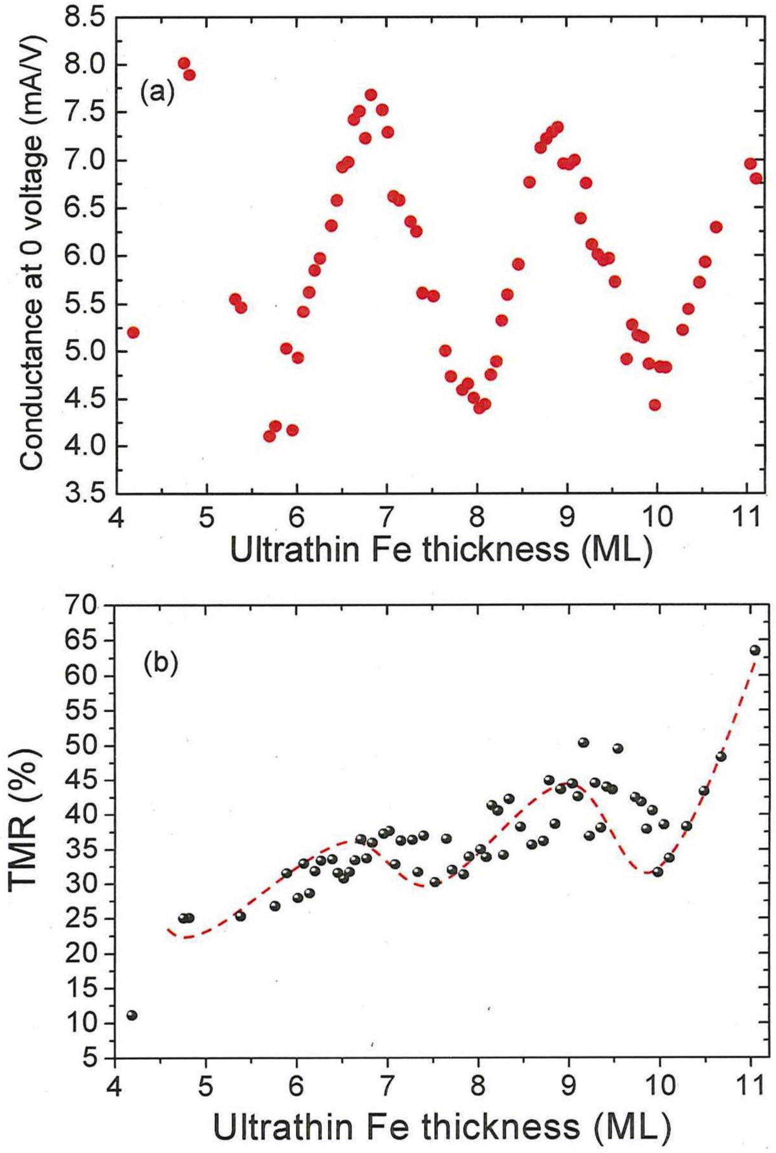

**Fig. 3.19**

(a) Ultrathin Fe thickness dependence of TMR and (b) conductance at parallel configuration. From (a) and (b), we can see the QW state influence on the TMR.

# CHAPTER4. CONCLUSIONS

To understand and realize control spin-dependent QW effect in MTJs with ultrathin Fe, the author focuses on the investigation in Cr/ultrathin Fe/MgO/Fe MTJs.

The author performed a detailed experimental study of spin-dependent quantum interference effects in MTJs with Fe QWs. Clear quantum interference effect in the sample fabricated by MBE was successfully observed. In agreement with QW theory, clear resonant peaks at different voltage were observed periodically with the change of Fe thickness. In addition, majority $\Delta_1$ band in the $\Gamma$ –H dispersion of bcc Fe deduced from experiment data of periodicity of resonant peak have a good agreement with first principle calculation. It convinced the observation of spin dependent QW state in ultrathin Fe.

However, a systematic discrepancy of 1 ML in the position of QW states was observed when comparing to ab initio calculation, which could be due to imperfect interfaces in samples. By using XAS/MCD, the possibility of Fe oxidization was ruled out. However, the presence of a 1.7±0.2 ML nonmagnetic layer was evidenced by MOKE, probably due to intermixing at the Fe/Cr interface. Intermixing may reduce the effective QW thickness by 1 ML, accounting for the author's transport results. This means that part of the Fe-Cr intermixed layer may become a barrier for $\Delta_1$ states. More theoretical work is needed to understand the exact influence of intermixing on the $\Delta_1$ band. Importantly, the author's results suggest that precisely controlling the Fe/Cr interface may be an efficient way to tune QW energies.

The influence of growth conditions and interface flatness on quantum well effect was also been investigated and discussed. A large enhancement of the conductance peak height was observed for the sample prepared by MBE with a post-annealing treatment at around 250 °C compared with the sample without annealing. The amplitude modulation ratio is as high as 150% for 6ML Fe thickness. It indicates the importance of interface flatness for QW effect.

Besides that, the differential MR also shows quantum well oscillations, and the oscillation phases are the same as those of conductivity. This is an indication of the QW effect on the spin-dependent transport. By controlling the QW state, one can enhance the TMR ratio under some voltages, which provides the potential application way to change the spintionics device performance.

# ACKNOWLEDAGEMENT

I would like to express my deepest appreciation to my Ph.D. supervisor Professor Yoshishige SUZUKI (professor, Osaka University, Japan), for his guidance, encouragement and persistent help I received throughout the research work. Professor SUZUKI has always made himself available to clarify my doubts despite his busy schedules. I am really grateful to his patient instruction and training by discussion of the experiment results and providing comments. I consider it as a great opportunity to do my doctoral study under his guidance and to learn from his research expertise.

I would also like to express my sincere gratitude to Dr. Frédéric BONELL (post doctor, Osaka University) for his significant contribution to my doctor research. He gave me a lot of knowledge of MBE experiment. In addition, I thank for his valuable suggestions and concise comments on data analysis.

I am also grateful to Dr. Takayuki NOZAKI (Researcher, AIST), Mr. Shinji MIWA (assistant professor, Osaka University) and Dr. Bang DO (post doctor, Toyota Technological Institute) for their useful advice for experiment skills and suggestion for some of the research papers of the thesis.

I am still thankful to Dr. Tetsuya Nakamura (Spring-8), for his professional support in XAS and MCD measurement.

I express my thanks to Professor Norikazu MIZUOCHI, Professor Teruya SHINJO, Dr. Eiichi TAMURA, for their selfless help in sharing their knowledge for my research.

I still wish to thank all of staff members in our lab at Osaka University. They are Ms. Yumi Oda, Ms. Rie HASEGAWA, Mrs. Kazuyo NAKAJIMA, Mr. Tadahiro SUGIMURA. Thank for their kind assistance and support. I also would also like to thank all other present and former members in Professor Suzuki's group, I can learned a lot from them.

I also would like to express my acknowledgement to Osaka University Global COE (G-COE) Program for funding my doctor thesis research work.

In the end, I sincerely thank my parents in China for their continuous support, understanding and encouragement.

# REFERENCES

[1] M. Julliere, Phys. Lett. A **54,** 225 (1975).

[2] T. Miyazaki and N. Tezuka, J. Magn. Magn. Mater. **139,** L231 (1995).

[3] J. S. Moodera, L. R. Kinder, T. M. Wong and R. Meservey, Phys. Rev. Lett. **74,** 3273 (1995).

[4] H. X. Wei, Q. H. Qin, M. Ma, R. Sharif, and X. F. Han, J. Appl. Phys. **101,** 09B501 (2007).

[5] W. H. Butler, X. G. Zhang, T. C. Schulthess, and J. M. MacLaren, Phys. Rev. B **63,** 054416 (2001).

[6] J. Mathon and A. Umerski, Phys. Rev. B **63**, 220403R (2001).

[7] S. Yuasa, T. Nagahama, A. Fukushima, Y. Suzuki and K. Ando, Nat. Mater. **3,** 868 (2004)

[8] S .S. P. Parkin, C. Kaiser, A. Panchula, P. M. Rice, B. Hughes, M. Samant and S. H. Yang Nat. Mater. **3,** 862 (2004)

[9] C. Tiusan, F. Greullet, M. Hehn, F. Montaigne, S. Andrieu and A. Schuhl, J. Phys.: Condens. Matter. **19,** 165201 (2007)

[10] S. Yuasa, J. Phys. Soc. Jpn. **77,** 031001 (2008)

[11] S. Yuasa, A. Fukushima, T. Nagahama, K. Ando, Y. Suzuki, Jpn. J. Appl. Phys. **43,** 588–590 (2004).

[12] T. Nagahama, S. Yuasa, Y. Suzuki, E. Tamura, J. Appl. Phys. **91,** 7035–7037 (2002).

[13] S. Yuasa, T. Nagahama, Y. Suzuki, Science. **297,** 234–237 (2002).

[14] T. Nozaki, N. Tezuka, K. Inomata, Phys. Rev. Lett. **96,** 027208 (2006).

[15] Y. Wang, Z.Y. Lu, X.G. Zhang, X.F. Han, Phys. Rev. Lett. **97,** 087210 (2006).

[16] F. Greullet, C. Tiusan, F. Montaigne, M. Hehn, D. Halley, O. Bengone, M. Bowen, W. Weber, Phys. Rev. Lett. **99,** 187202 (2007).

[17] T. Niizeki, N. Tezuka, K. Inomata, Phys. Rev. Lett. **100,** 047207 (2008).

[18] A. lovan, S. Andersson, Yu.G. Naidyuk, A. Vedyaev, B. Dieny, V. Korenivski, Nano. Lett. **8,** 805–809 (2008).

[19] D. Bang, T. Nozaki, Y. Suzuki, J. Appl. Phys. **109,** 07C719 (2011).

[20] Z.Y. Lu, X.G. Zhang, S.T. Pantelides, Phys. Rev. Lett. **94,** 207210 (2005).

[21] T. Nozaki, Y. Jiang, Y. Kaneko, A. Hirohata, N. Tezuka, S. Sugimoto, and K. Inomata, Phys. Rev. B **70,** 172401 (2004).

[22] R. K. Kawakami, E. Rotenberg, Hyuk J. Choi, Ernesto J. Escorcia-Aparicio, M. O. Bowen, J. H. Wolfe, E. Arenholz, Z. D. Zhang, N. V. Smith and Z. Q. Qiu, Nature **398,** 11 (1999).

[23] H. L. Meyerheim, R. Popescu, J. Kirschner, N. Jedrecy, M. S. Simkin, B. Heinrich, and R. Pinchaux, Phys. Rev. Lett. **87,** 076102 (2001).

[24] X. G. Zhang, W. H. Butler, and A. Bandyopadhyay, Phys. Rev. B **68,** 092402 (2003).

[25] C. Zhang, X. G. Zhang, P. S. Krstić, H. P. Cheng, W. H. Butler, and J. M. MacLaren, Phys. Rev. B **69,** 134406 (2004).

[26] S. G. Wang, R. C. C. Ward, T. Hesjedal, X.G. Zhang, C. Wang, A. Kohn, Q. L. Ma, J. Zhang, H. F. Liu, and X. F. Han, J NANOSCI NANOTECHNO. **12,** 1006–1023 (2012)

[27] H. Oh, S. B. Lee, H. G. Min, and J.S. Kim, Appl. Phys. Lett. **82,** 361 (2003)

[28] F. J. Palomares, C. Munuera, C. M. Boubeta, and A. Cebollada, J. Appl. Phys. **97,** 036104 (2005).

[29] M. Sicot, M. Andrieu, P. Turban, Y. Fagot-Revurat, H. Cercellier, A. Tagliaferri, C. de Nadai, N. B. Brookes, F. Bertran, and F. Fortuna, Phys. Rev. B **68,** 184406 (2003).

[30] K. Miyokawa, S. Saito, T. Katayama, T. Saito, T. Kamino, K. Hanashima, Y. Suzuki, K. Mamiya, T. Koide, and S. Yuasa, Jpn. J. Appl. Phys. **44,** L9 (2005).

[31] M. Müller, F. Matthes, and C. M. Schneider, Europhys. Lett. **80,** 17007 (2007).

[32] D. Telesca, B. Sinkovic, S.H. Yang, S.S.P. Parkin, J. Electron. Spectrosc. Relat. Phenom. **185,** 133- 139 (2012).

[33] P. J Zermatten, F. Bonell, S. Andrieu, M. Chshiev, C. Tiusan, A. Schuh, and G. Gaudin, Appl. Phys. Express **5,** 023001 (2012).

[34] Y. J. Choi, I. C. Jeong, J.Y. Park, S. J. Kahng, J. Lee, and Y. Kuk, Phys. Rev. B **59,** 10918 (1999).

[35] R. Ravlic, M. Bode and R. Wiesendanger, J. Phys.: Condens. Matter. 15, S2513-S2531 (2003).

[36] T. Kawagoe, Y. Iguchi, T. Miyamachi, A. Yamasaki and S. Suga, Jpn. J. Appl. Phys. **45,** 2234–2237 (2006).

[37] J.G. Simons, J. Appl. Phys. **34,** 238–239 (1963).

[38] J. Stöhr, J. Electron. J. Electron. Spectrosc. Relat. Phenom. **75,** 53-272 (1995).

[39] N. V. Smith, N. B. Brookes, Y. Chang and P. D. Johnson, Phys. Rev. B **49,** 332 (1994).

[40] Y. Z. Wu, C. Y. Won, E. Rotenberg, H. W. Zhao, F. Toyoma, N. V. Smith and Z. Q. Qiu, Phys. Rev. B **66,** 245418 (2002).

[41] A. Enders, T. L. Monchesky, K. Myrtle, R. Urban, B. Heinrich, J. Kirschner, X.-G. Zhang, and W. H. Butler, J. Appl. Phys. **89,** 7110 (2001).

[42] T. J. Regan, H. Ohldag, C. Stamm, F. Nolting, J. Lüning, J. Stöhr and R. L. White, Phys. Rev. B **64,** 214422 (2001).

[43] F. Bonell, S. Andrieu, A. M. Bataille, C. Tiusan, and G. Lengaigne, Phys. Rev. B **79,** 224405 (2009).

[44] C.A.F. Vaz, J.A.C. Bland, and G. Lauhoff, Rep. Prog. Phys. **71,** 056501 (2008).

[45] I. G. Kim, J. I. Lee, Y.R. Jang and S. C. Hong, J. Korean Phys. Soc **31,** 491-494 (1997).

[46] S. Mirbt, I. A. Abrikosov, and B. Johansson and H. L. Skriver, Phys. Rev. B **55,** 67-69,

(1997).

[47] M. Sicot, S. Andrieu, F. Bertran, F. Fortuna, Phys. Rev. B **72,** 144414 (2005).

[48] A. Froideval, R. Iglesias, M. Samaras, S. Schuppler, P. Nagel, D. Grolimund, M.Victoria, and W. Hoffelner, Phys. Rev. Lett. **99,** 237201 (2007).

[49] J. E. Ortega and F. J. Himpsel, Phys. Rev. Lett. **69,** 844 – 847 (1992)

[50] Z. Q. Qiu and N. V. Smith, J. Phys.: Condens. Matter **14,** R169–R193 (2002)

[51] M. Milun, P. Pervan and D. P. Woodruff, Rep. Prog. Phys. **65,** 99–141 (2002)

[52] R. Matsumoto, A. Fukushima, T. Nagahama, Y. Suzuki, K. Ando, S. Yuasa, Appl. Phys. Lett. **90,** (2007) 252506.

# List of Publications

1. P. Sheng, Do Bang, T. Nozaki, S. Miwa, Y. Suzuki,
   Spin-dependent quantum well effect in fully epitaxial Cr/ultrathin Fe/MgO/Fe magnetic tunnel junctions,
   Solid State Communications **152,** 273–277 (2012)

2. P. Sheng, F. Bonell, S. Miwa, T. Nakamura, Y. Shiota, S. Murakami, D. D. Lam, S. Yoshida, Y. Suzuki
   Detailed Analysis of Spin-Dependent Quantum Interference Effects in Magnetic Tunnel Junctions with Fe Quantum Wells,
   Appl. Phys. Lett. **102,** 032406 (2013)

# List of Conference Presentations

1. B. Do, P. Sheng, T. Nozaki and Y. Suzuki,
   Spin-Dependent Quantum Interference Effect in Fully Epitaxial Cr/Ultrathin-Fe/MgO/Fe Magnetic Tunnel Junctions (poster presentation)
   International Conference of Asian Union of Magnetics Societies (ICAUMS), Jeju, Korea, Dec.2010.

2. P. Sheng, D. Bang, T. Nozaki and Y. Suzuki,
   Spin-Dependent Quantum Well Effect in Fully Epitaxial Cr/Ultrathin-Fe/MgO/Fe Magnetic Tunnel Junctions (poster presentation)
   IEEE International Magnetics Conference (Intermag), Taipei, China. April. 2011.

3. P. Sheng, T. Nozaki and Y. Suzuki,
   Spin Related Quantum Well Effect in Fully Epitaxial Cr/ultrathin-Fe/MgO/Fe Magnetic Tunnel Junctions (oral presentation)
   56th Annual Conference on Magnetism and Magnetic Materials (MMM), Scottsdale, USA. November, 2011.

4. P. Sheng, F. Bonell, S. Miwa, T. Nakamura, Y. Shiota, S. Murakami, D. D. Lam, S. Yoshida, and Y. Suzuki,
   Observation of Spin-Dependent Quantum Interference Effects in Magnetic Tunnel Junctions with Fe Quantum Wells (poster presentation)
   The 21st International Colloquium on Magnetic Films and Surfaces (ICMFS), Shanghai, China. September, 2012